Chapter 3

Pulse propagation in 2-D and 3-D random media

Summary

In this chapter the main results of the thesis are presented. It is shown how the generalized O'Doherty-Anstey approach of Shapiro and Hubral (1999) can be extended to the case of 2-D and 3-D random media. That is to say the primary wave field is approximated with help of a second-order Rytov approximation combined with the Bourret approximation and the causality principle. The self-averaging property of logarithmic wave field attributes can be also observed in 2-D (3-D) random media. As a consequence the extended ODA approach describes most probable pulses in single realizations of the random medium. Moreover, expressions for the scattering attenuation coefficient and the phase velocity for plane and spherical waves are obtained. Based on these wave field attributes the Green's function for the primary wave field is constructed. In the long travel-distance limit, an explicit result in the form of a Gaussian pulse is obtained. Parts of this chapter are published in Müller and Shapiro (2001a) and Müller et al. (2001).

Section (3.1) contains a brief outline of the O'Doherty-Anstey theory in 1-D random media. Then, the analogous strategy will be applied to 2-D and 3-D random media. It turns out that additionally the causality principle must be applied in order to obtain full frequency range wave field attributes (see section (3.2)-(3.4)). That self-averaging takes place in 2-D random media is demonstrated in section (3.5). Section (3.6) provides a detailed discussion of the attenuation and phase velocity dispersion derived in that way. In section (3.7) the Green's function corresponding to the primary wave field is formulated. Finally, the results are numerically verified in section (3.8).

3.1 Review of the ODA approach in 1-D random media

For 1-D random media, Shapiro & Hubral (1999) approximated the transmitted wave field with help of a second-order Rytov approximation. An essential feature of their wave field description is its ability to describe the wave field in a single realization of the random medium. That is to say, it is an approximation of non-averaged wave fields. This is possible due to the use of self-averaged wave field attributes. The latter are quantities that assume their ensemble averaged values when propagating in a single realization of the random medium. Shapiro & Hubral indeed showed the self-averaging of the phase increment and the attenuation coefficient.

For a sound wave vertically impinging on a stack of randomly distributed layers (for simplicity we assume the density to be constant) the time-harmonic transmissivity can be written

$$T(t,\omega) = e^{-\alpha^{1D}L + i\varphi^{1D}L}\, e^{-i\omega t} \tag{3.1}$$

with

$$\alpha^{1D} = k^2 \int_0^\infty dr\, B_a(r) \cos(2kr) \tag{3.2}$$

$$\varphi^{1D} = k^2 + kB_a(0) - k^2 \int_0^\infty dr\, B_a(r) \sin(2kr)\,, \tag{3.3}$$

where k denotes the wave number, $B_a(r)$ the velocity correlation function. The quantities α^{1D} and φ^{1D} are called the attenuation coefficient and the phase increment, respectively. Equation (3.1) corresponds to equation (4.18) in Shapiro and Hubral (1999).

Noting the relationship between the correlation function and its (1-D) Fourier transform

$$B_a(r) = \frac{1}{\pi} \int_0^\infty d\zeta\, \Phi(\zeta) \cos(\zeta r) \tag{3.4}$$

equation (3.2) can be written

$$\alpha^{1D} = \frac{k^2}{\pi} \int_0^\infty dr \int_0^\infty d\kappa\, \Phi(\kappa) \cos(\kappa r) \cos(2kr) \tag{3.5}$$

$$= \frac{k^2}{2} \int_0^\infty d\kappa\, \Phi(\kappa) \left[\delta(\kappa + 2k) + \delta(\kappa - 2k)\right] \tag{3.6}$$

$$= \frac{k^2}{2}\, \Phi(2k)\,. \tag{3.7}$$

This corresponds to equation (3.1) in Samelsohn et al. (1999) (apart from a factor π because a different definition of the Fourier transform is used) and is a known result from localization theory. The localization length is then $\gamma = 1/\alpha^{1D}$. That only the $2k$ components of the fluctuation spectrum are responsible for the localization of a wave with wave number k can be physically interpreted in terms of Bragg scattering in quasi-periodic media using the Ewald sphere construction (Samelsohn et al., 1999).

Moreover, it can be shown that α^{1D} and φ^{1D} are related by a pair of Hilbert transforms expressing the causality of the wave field.

Both wave field attributes are self-averaged quantities. That is to say in any typical realization of the random medium, α^{1D} and φ^{1D} converge to the same values when the travel-distance tends to infinity. For finite travel-distances L, it can be shown that the relative fluctuations of α^{1D} and φ^{1D} vanish like $1/\sqrt{L}$ indicating that the process of self-averaging takes place.

The transient transmissivity i.e. the signal when a δ-pulse enters into the random medium (we call this later the medium's Green function) can be obtained by an inverse Fourier transform of equation (3.1). In the case of exponential and Gaussian correlation functions explicit results can be obtained. In the long travel-distance limit this signal is approximately a Gaussian pulse.

In the following we generalize these ideas to the case of wave propagation in 2-D and 3-D random media. This strategy leads to the extended O'Doherty-Anstey theory.

3.2 Extension of the ODA theory to 2-D and 3-D media

We look for a solution of the wave equation (2.1) in the form of a time-harmonic plane wave $u(t,\omega)$. We describe the wave field inside the random medium with help of the Rytov transformation, using the complex exponent $\Psi = \chi + i\phi$, where the real part χ represents the fluctuations of the logarithm of the amplitude – the log-amplitude fluctuations – and the imaginary part ϕ represents phase fluctuations (compare with section 2.1.3). Omitting the time dependence $\exp(-i\omega t)$, we write

$$u(t,\omega,\mathbf{r}) \quad = \quad U_0(\omega,\mathbf{r}) e^{\chi(\omega,\mathbf{r})+i\phi(\omega,\mathbf{r})}\,, \tag{3.8}$$

where $U_0 = A_0 \exp(i\phi_0)$ is the wave field in the homogeneous reference medium ($n(\mathbf{r}) = 0$) with the amplitude A_0 and the unwrapped phase ϕ_0. To be more specific, we assume that the initially plane wave propagates vertically along the z-axis. Equation (3.8) can then be written

$$u(t,\omega,z=L,\mathbf{r}_\perp) = e^{iK(\omega,L,\mathbf{r}_\perp)L}\,, \tag{3.9}$$

where we introduced the complex wave number

$$K(\omega,L,\mathbf{r}_\perp) \quad = \quad \left(\frac{\phi(\omega,L,\mathbf{r}_\perp)}{L} + \frac{\phi_0(\omega,L)}{L}\right) - i\frac{\chi(\omega,L,\mathbf{r}_\perp)}{L} \tag{3.10}$$

$$= \quad \varphi(\omega,L,\mathbf{r}_\perp) + i\alpha(\omega,L,\mathbf{r}_\perp)\,, \tag{3.11}$$

with real functions φ and α denoting the phase increment and attenuation coefficient, respectively. L is the travel-distance and $\mathbf{r}_\perp$ denote the transverse coordinates relative to the z-axis.

By analogy with the generalized ODA formalism in the 1-D case, we use the wave field approximation in 2-D and 3-D:

$$u(t,\omega,L,\mathbf{r}_\perp) \approx e^{i[\langle\varphi\rangle+i\langle\alpha\rangle]L} \quad . \tag{3.12}$$

Note that equation (3.12) is expected to describe the wave field in single realizations of random media, since its lefthand side is not subjected to statistical averaging. The righthand side contains, however, the ensemble averaged wave field attributes $\langle\varphi\rangle$ and $\langle\alpha\rangle$. To keep equation (3.12) physically true, we require self-averaging of the quantities α and φ. In the following we consider the approximations and properties of the logarithmic wave field attributes $\langle\chi\rangle$ and $\langle\phi\rangle$. In section (3.5) we study the self-averaging property of α and φ. It turns out that for finite travel-distances, only a partial self-averaging can be reached.

3.3 Approximation for the logarithmic wave field attributes

We derive now tractable approximations for the wave field attributes $\langle\chi\rangle$ and $\langle\phi\rangle$ in the weak wave field fluctuation regime. To do so we note that the wave field can be separated into a coherent and fluctuating (incoherent) part: $u = \langle u\rangle + u_f$ where $\langle u\rangle$ denotes the ensemble averaged wave field. A measure of the wave field fluctuations is the ratio

$$\varepsilon = \left|\frac{u_f}{\langle u\rangle}\right| \quad , \tag{3.13}$$

whose variance is given by $\langle\varepsilon^2\rangle = \frac{I_t}{I_c} - 1$, where $I_t = \langle|u|^2\rangle$ is the total intensity and $I_c = |\langle u\rangle|^2$ is the coherent intensity. Then, the range of weak fluctuation is defined by $\langle\varepsilon^2\rangle \ll 1$ and means that the coherent intensity is of the order of the total intensity.

From equation (3.8) we see that the fluctuations of amplitude and phase due to the presence of inhomogeneities are then described by the functions

$$\begin{aligned} \chi &= \ln\left|\frac{u}{U_0}\right| \\ \phi &= -i\ln\left(\frac{u}{U_0}\left|\frac{U_0}{u}\right|\right) \quad . \end{aligned} \tag{3.14}$$

If we make use of equation (3.13), neglect terms higher than $\mathcal{O}(\varepsilon^2)$ and average, we obtain from equations (3.14)

$$\begin{aligned} \langle\chi\rangle &= \ln\left|\frac{\langle u\rangle}{U_0}\right| - \frac{1}{4}\langle\varepsilon_u^2 + \varepsilon_u^{\star 2}\rangle \\ \langle\phi\rangle &= \phi_c - \phi_0 + \frac{i}{4}\langle\varepsilon_u^2 - \varepsilon_u^{\star 2}\rangle \quad , \end{aligned} \tag{3.15}$$

where $\varepsilon_u = u_f/\langle u\rangle$ so that $|\varepsilon_u| = \varepsilon$ and $\varepsilon^\star$ means the complex conjugated quantity. Further, the coherent wave field may be represented as $\langle u\rangle = \sqrt{I_c}\exp(i\phi_c)$; ϕ_c denotes the coherent phase. When we calculate the variance (crossvariance) of these quantities and neglect again terms of order higher than $\mathcal{O}(\varepsilon^2)$, we find:

$$\begin{aligned} \sigma_{\chi\chi}^2 &= \frac{1}{4}\langle(\varepsilon_u + \varepsilon_u^\star)^2\rangle = -\ln\left|\frac{\langle u\rangle}{U_0}\right| + \frac{1}{4}\langle\varepsilon_u^2 + \varepsilon_u^{\star 2}\rangle \\ \sigma_{\chi\phi}^2 &= \frac{i}{4}\langle\varepsilon_u^2 - \varepsilon_u^{\star 2}\rangle \quad . \end{aligned} \tag{3.16}$$

Comparing equations (3.15) and (3.16), the averaged fluctuations of amplitude and phase due to the presence of inhomogeneities can be described by (see also Shapiro and Kneib, 1993, and Shapiro et al., 1996b)

$$\langle\chi\rangle = -\sigma_{\chi\chi}^2 + \mathcal{O}(\varepsilon^3) \quad , \tag{3.17}$$

$$\langle\phi\rangle = \phi_c - \phi_0 - \sigma_{\chi\phi}^2 + \mathcal{O}(\varepsilon^3) \quad . \tag{3.18}$$

These are useful relations since all quantities on the righthand side can be obtained in the well-known Rytov- and Bourret approximation. More precisely, the log-amplitude variance $\sigma_{\chi\chi}^2$ and the log-amplitude phase crossvariance $\sigma_{\chi\phi}^2$ can be calculated with help of the Rytov approximation. The coherent phase ϕ_c follows from the Bourret approximation. Note that equation (3.17) and (3.18) can be derived either by restricting to the weak fluctuation regime

or by assuming normally distributed χ and ϕ. However in both cases, the derivation of equation (3.17) is based on the assumption that the total intensity remains constant. Conversely, in order to derive equation (3.18) no assumption for I_t has to be made.

In appendix B we provide the explicit expressions for $\sigma^2_{\chi\chi}, \sigma^2_{\chi\phi}, \phi_c$ in 2-D and 3-D random media. To stress the analogy to the 1-D case, where a second-order Rytov approximation has been applied, we provide an alternative derivation of equation (3.17), which is also based on the second-order Rytov approximation in appendix A.2.

3.4 Causality

It is the purpose of this section to construct logarithmic wave field attributes which satisfy the Kramers-Kronig relationship. That means the ballistic wave field in random media obeys the causality principle. Kramers-Kronig relations are based upon the physical constraint that the response of any medium must be causal. For a comprehensive review of this topic we refer to Beltzer (1989) and Weaver & Pao (1981). The Kramers-Kronig relations provide a rather general tool to investigate wave propagation in heterogeneous media (e.g. Beltzer (1985), Beltzer et al. (1990), and Fang & Müller (1996)).

3.4.1 Causal wave field attributes

The Kramers-Kronig equations allow to reconstruct the attenuation from the dispersion behavior and vice versa since both quantities are related by a pair of Hilbert transforms. To this end it is sufficient to derive a Kramers-Kronig relationship for the complex wave number $K(\omega)$ of the plane wave response. For our purpose it is expedient to use the formulation of the Kramers-Kronig relationship of Weaver and Pao (1981). We do not re-derive the Kramers-Kronig relationship from the very beginning but rather start with their main result for twice-subtracted dispersion relations (see their equations (71) and (72) and appendix C.1):

$$\varphi(\omega') = B\omega' + \frac{2\omega'}{\pi}\int_0^\infty \frac{\alpha(\omega)-\alpha(\omega')}{\omega^2-\omega'^2}\,d\omega + \varphi(0) \tag{3.19}$$

$$\alpha(\omega') = \frac{-2\omega'^2}{\pi}\int_0^\infty \left[\frac{\varphi(\omega)}{\omega} - \frac{\varphi(\omega')}{\omega'}\right]\frac{d\omega}{\omega^2-\omega'^2} + \alpha(0) \tag{3.20}$$

where $B = \lim_{\omega\to\infty}\alpha(\omega)/\omega$.

In the following we derive the scattering attenuation coefficient α by applying equation (3.20) to the phase increment (equation (3.18) divided by the travel-distance). Let's begin with the Rytov part of the phase increment, i.e. $-\sigma^2_{\chi\phi}$ which is in 3-D random media given by equation (B.2). Inserting equation (B.2) into equation (3.20) we get

$$\begin{aligned}\alpha_R(\omega') &= \frac{2\omega'^2}{\pi}\int_0^\infty d\omega\,\frac{\sigma^2_{\chi\phi}(\omega)}{\omega(\omega^2-\omega'^2)} - \frac{2\omega'^2}{\pi}\frac{\sigma^2_{\chi\phi}(\omega')}{\omega'}\int_0^\infty d\omega\,\frac{1}{(\omega^2-\omega'^2)} \\ &= \frac{2\omega'^2}{\pi}\int_0^\infty d\omega\,\frac{c_1\omega^2\int_0^\infty d\kappa\,\Phi(\kappa)/\kappa\,\sin^2(c_2/\omega)}{\omega^2-\omega'^2} - i\sigma^2_{\chi\phi}(\omega')\,,\end{aligned} \tag{3.21}$$

where we used $\int_0^\infty d\omega\,\frac{1}{\omega^2-\omega'^2} = \frac{i\pi}{2}\frac{1}{\omega'}$ and set $c_1 = 4\pi^2/(Lc_0^3)$, $c_2 = \kappa^2 L c_0/2$. Changing the order of integration and integrate with respect to ω, we find

$$\alpha_R(\omega') = c_1\omega'^2\int_0^\infty d\kappa\,\frac{\Phi(\kappa)}{\kappa}\left[c_2 - \frac{1}{2}\omega'\sin\left(\frac{2c_2}{\omega}\right) + i\left(\frac{1}{2}\omega' - \frac{1}{2}\omega'\cos\left(\frac{2c_2}{\omega}\right)\right)\right]$$

$$-i\sigma^2_{\chi\phi}(\omega')\,. \tag{3.22}$$

Using trigonometric relations it is easy to see that the imaginary parts cancel out. The remaining real part is

$$\begin{aligned}\alpha_R(\omega') &= 2\pi^2\frac{\omega'^2}{c_0^2}\int_0^\infty d\kappa\,\kappa\,\Phi(\kappa)\left[1-\frac{\sin(\kappa^2 Lc_0/\omega')}{\kappa^2 Lc_0/\omega'}\right] &(3.23)\\ &= \frac{\sigma^2_{\chi\chi}(\omega')}{L}\,. &(3.24)\end{aligned}$$

Thus, the Rytov parts of equations (3.17) and (3.18) are related by the Kramers-Kronig relationship.

Now the questions arises, what happens with the Bourret part of equation (3.18), namely ϕ_c, when subjected to the Kramers-Kronig dispersion relations? We show that this results in an additional attenuation term α_B. To do so, we note that the phase increment resulting from the Bourret approximation can be written

$$\begin{aligned}\varphi_c(\omega') &= \phi_c(\omega')/L\\ &= \frac{\omega'}{c_0}+\frac{\omega'^2}{c_0^2}\int_0^\infty dr\,\sin(2\omega'/c_0 r)B(r)\,. &(3.25)\end{aligned}$$

Inserting equation (3.25) into equation (3.20) we obtain

$$\begin{aligned}\alpha_B(\omega') &= -\frac{2\omega'^2}{\pi}\int_0^\infty d\omega\,\frac{\varphi_c(\omega)}{\omega(\omega^2-\omega'^2)}+\frac{2\omega'^2}{\pi}\frac{\varphi_c(\omega')}{\omega'}\int_0^\infty d\omega\,\frac{1}{(\omega^2-\omega'^2)}\\ &= -\frac{2\omega'^2}{\pi}\left[\frac{1}{c_0}\int_0^\infty d\omega\,\frac{1}{(\omega^2-\omega'^2)}+\frac{1}{c_0^2}\int_0^\infty dr\,B(r)\int_0^\infty d\omega\,\frac{\omega}{\omega^2-\omega'^2}\sin(2\omega r/c_0)\right]\\ &\quad +i\varphi_c(\omega')\\ &= -\omega'^2\left[\frac{1}{c_0}\frac{i}{\omega'}+\frac{1}{c_0^2}\int_0^\infty dr\,B(r)\left(\cos(2\omega' r/c_0)+i\cos(2\omega' r/c_0)\right)\right]+i\varphi_c(\omega')\,.\end{aligned}$$

Again, it is easy to verify that the imaginary parts cancel out and the real part simplifies to

$$\alpha_B(\omega') = 2\frac{\omega'^2}{c_0^2}\int_0^\infty B(r)\sin^2(\omega' r/c_0)dr-\frac{\omega'^2}{c_0^2}\int_0^\infty B(r)dr\,. \tag{3.26}$$

To put equation (3.26) into a more compact form we note that in isotropic random media the correlation function and fluctuation spectrum are related by (see e.g. Rytov et al., 1989)

$$B(r)=\frac{4\pi}{r}\int_0^\infty \Phi(\kappa)\sin(\kappa r)\,\kappa\,d\kappa\,. \tag{3.27}$$

Thus, equation (3.26) becomes

$$\begin{aligned}\alpha_B(\omega') &= 8\pi k^2\int_0^\infty d\kappa\,\Phi(\kappa)\,\kappa\int_0^\infty dr\frac{\sin^2(kr)\sin(\kappa r)}{r}-4\pi k^2\int_0^\infty d\kappa\,\Phi(\kappa)\int_0^\infty dr\frac{\sin(\kappa r)}{r}\\ &= 2\pi^2k^2\left[\int_0^\infty d\kappa\,\Phi(\kappa)-\int_{2k}^\infty d\kappa\,\Phi(\kappa)-\int_0^\infty d\kappa\,\Phi(\kappa)\right]\\ &= -2\pi^2k^2\int_{2k}^\infty d\kappa\,\Phi(\kappa)\kappa\,, &(3.28)\end{aligned}$$

where $k=\omega'/c_0$.

To summarize, we derived two pairs of wave field attributes, $\{\sigma^2_{\chi\chi}, -\sigma^2_{\chi\phi}\}$ and $\{\alpha_B L, \phi_c - \phi_0\}$, each of them related by (3.20). Therefore, the causality principle suggests to use the following logarithmic wave field attributes in 2-D as well as 3-D random media:

$$\langle\chi\rangle = -(\alpha_R + \alpha_B)L = -\sigma^2_{\chi\chi} - \alpha_B L \quad , \tag{3.29}$$

$$\langle\phi\rangle = \phi_c - \phi_0 - \sigma^2_{\chi\phi} \quad . \tag{3.30}$$

In the next section we discuss the validity range for these wave field attributes. Note that we used in equations (3.23)-(3.28) the 3-D wave field attributes. Applying the same strategy to derive the 2-D wave field attributes fails. This is because the coherent phase in 2-D is of the order $\mathcal{O}(\omega^3)$ and application of equation (3.20) results in a diverging integral. A higher-order dispersion relation has to be used as shown in appendix C.2. Then, it is possible to obtain an approximation of α_B in the form of (3.28) and equation (3.29) can be also used for 2-D random media.

It is interesting to note that in the above derivation of equation (3.29) no assumption concerning the total intensity has been made (see once more the comments after equation (3.18)).

3.4.2 Validity range

In order to analyze the different propagation regimes, it is common to introduce the so-called wave parameter $D = \frac{2L}{ka^2}$ where a is the characteristic length of the heterogeneities (see also section 2.1.2). Thus, $D \gg 1$ describes the diffraction regime, whereas $D \ll 1$ denotes the geometrical optics regime.
In equations (3.29), (3.30) the quantities $\sigma^2_{\chi\chi}$ and $\sigma^2_{\chi\phi}$ are obtained in the Rytov approximation. The latter is restricted to small wave field fluctuations. That is to say $\sigma_n^2 < 1$ and $\sigma^2_{\chi\chi} < 1$. It is further assumed that forward scattering dominates and therefore $ka > 1$.

In the literature, the validity range of the Bourret approximation, which is applied in order to compute the coherent phase ϕ_c, is given by $\sigma_n^2(ka)^2 < 1$ (see e.g. equation (4.52) of Rytov et al., 1989). Recently, Samelsohn and Mazar (1996) showed by the path integral approach that the Bourret approximation has a wider range of applicability. They provide the less stringent restriction $ka^2 \ll L$ or equivalently $D \gg 1$. Moreover, even if this condition fails, the linear combination of ϕ_c and $\sigma^2_{\chi\phi}$ in equation (3.30) makes sense. This becomes clear when we consider the behavior of ϕ_c as given in equations (B.10) and (B.9) for $ka \to \infty$. One can show that ϕ_c tends to zero in this limit. That is for large ka the Bourret approximation of ϕ_c yields wrong results, however, they become insignificantly small compared with $\sigma^2_{\chi\phi}$. On the other hand, for $ka \to 0$ the Bourret approximation holds, whereas $\sigma^2_{\chi\phi}$ can be neglected.

The validity range of equation (3.29) is obtained by the following reasoning. The physical constraint to make equation (3.29) valid is obviously given by a non-negative attenuation coefficient, i.e., $\alpha = \alpha_R + \alpha_B \geq 0$. Taking into account equations (B.1) and (3.28) the aforesaid constraint implies

$$\int_0^{4k^2a^2} d\kappa\, \Phi(\sqrt{\kappa}/a) \geq \int_0^{\infty} d\kappa\, \frac{\sin(\kappa D/2)}{\kappa D/2}\, \Phi(\sqrt{\kappa}/a)\,. \tag{3.31}$$

Since the fluctuation spectrum $\Phi(\kappa)$ is by definition a positive but monotonically decreasing function, the lefthand-side integral is bounded from below by $4k^2a^2\Phi(\sqrt{4k^2a^2}/a)$ and we can

write a stronger condition

$$4k^2a^2\Phi(2k) \geq \int_0^\infty d\kappa \, \frac{\sin(\kappa D/2)}{\kappa D/2} \, \Phi(\sqrt{\kappa}/a) \, . \tag{3.32}$$

Noting that $D = 2\frac{L}{a}/(ka)$, we can rewrite the last equation as

$$\left(\frac{L}{a}\right)^2 \geq D \left[\frac{1}{8}\int_0^\infty d\kappa \, \frac{\sin(\kappa D/2)}{\kappa} \frac{\Phi(\sqrt{\kappa}/a)}{\Phi(2k)}\right] . \tag{3.33}$$

The term in rectangular brackets is for most fluctuation spectra bounded by unity. Therefore, we obtain the validity range in terms of the wave parameter

$$\frac{1}{\pi L/\lambda} \leq D \leq \left(\frac{L}{a}\right)^2 \tag{3.34}$$

if $L > \max\{\lambda, a\}$ and λ denotes the wavelength. The latter condition is a consequence of the use of self-averaging as discussed in the following section (see comments after equation (3.38)). A similar analysis can be done for the 2-D case yielding the same result. For seismology, equation (3.34) is not a strong restriction. There, a typically ranges from several $10m$ to 10^3m and the wavelength is several $100m$. However, the travel-distance is of the order of 10^5m. In the field of exploration geophysics, one usually deals with a from $1m$ to several $10m$, the wavelength denotes several $10m$ and the travel-distances are up to 10^4m.

3.5 Self-averaging

Our goal is to describe the ballistic wave field in single realizations of the random medium. As pointed out in section (3.2), this requires the self-averaging of the logarithmic wave field attributes α and φ. A self-averaged quantity tends to its mathematical expectation value provided that the wave has covered a sufficient large distance inside the medium. So, their values in a particular realization coincide with the ensemble averaged value. Self-averaging of extensive physical quantities is a fundamental property of disordered media. A sound investigation of the self-averaging phenomena can be found in Lifshits et al. (1988). For 1-D random media, Shapiro and Hubral showed that the attenuation coefficient as well as the vertical phase increment of the transmissivity are such self-averaged quantities.

3.5.1 Partial self-averaging

For 2-D and 3-D random media, we show that the attenuation coefficient α and the phase increment φ in the above discussed approximations tend to their expectation values for increasing travel-distances. Lifshits et al. (1988) pointed out that the disappearance of the relative fluctuations of a quantity in the macroscopic limit is an indication of self-averaging. In our context the macroscopic limit corresponds to the limit $L \to \infty$. Therefore, we compute the relative standard deviations of the attenuation coefficient and phase increment and provide the estimates

$$\frac{\sigma_\alpha}{\alpha} \approx \frac{\sqrt{\sigma^2_{\chi\chi}}}{\langle\chi\rangle} \tag{3.35}$$

$$= \frac{1}{\sqrt{\sigma^2_{\chi\chi}}} \propto \sqrt{\frac{1}{L}} \tag{3.36}$$

$$\frac{\sigma_\varphi}{\varphi} = \frac{\sqrt{\langle\phi^2\rangle - \langle\phi\rangle^2}}{\langle\phi\rangle + \phi_0} \tag{3.37}$$

$$\approx \frac{\sqrt{\sigma^2_{\phi\phi}}}{\phi_0} \propto \sqrt{\frac{1}{L}} \quad , \tag{3.38}$$

where $\sigma^2_{\phi\phi}$ is given in equation (B.3). It is obvious that for increasing travel-distance, the relative standard deviations decrease like $1/\sqrt{L}$ and therefore the process of self-averaging takes place. For $L \to \infty$ the relative standard deviation would vanish. Note, however, that for finite L, which is a necessary condition to stay within the weak wave field fluctuation regime, $\frac{\sigma_\alpha}{\alpha}$ and $\frac{\sigma_\varphi}{\varphi}$ are nonzero. Therefore, only a partial self-averaging can be reached. We conclude that the logarithmic wave field quantities under consideration are partially self-averaged quantities at least in the weak wave field fluctuation range and for $L/a > 1$.

Equations (3.36) and (3.38) along with the results of numerical finite-difference experiments are plotted in Figure (3.1) and Figure (3.2) versus the travel-distance for an exponentially correlated random medium. The attenuation coefficient α is numerically determined by taking the logarithm of $A(\omega_0)$ divided by the travel-distance, i.e., the value of the amplitude spectrum at the fundamental frequency of the input-wavelet (the amplitude spectrum is calculated for a constant time window). It is obvious that for increasing travel-distance, the relative standard deviations decrease like $1/\sqrt{L}$ and therefore the process of self-averaging takes place. Note that for small travel-distances, the relative standard deviation of the attenuation coefficient falls off with L^{-1} since α is here proportional to L^2 (consider equation (B.1) for $L \to 0$). We conclude that the logarithmic wave field quantities under consideration are self-averaged quantities at least in the weak wave field fluctuation range.

An additional numerical demonstration of self-averaging is given in Figures (3.3) and (3.4), where we use the results of plane wave transmission simulations in 2-D elastic random media. We consider the simulated attenuation coefficient and traveltime fluctuations versus the spatial position transverse to the main propagation direction for different travel-distances L,respectively. Fig. (3.3) shows the relative fluctuations of the attenuation coefficient computed from the seismograms at 54 geophones along receiver-lines located at three different depths inside the random medium. We clearly observe that for increasing travel-distances, the relative fluctuations decrease. In the same way, Figure (3.4) shows the decrease of the relative fluctuations of the traveltimes $\sqrt{\sigma_t^2}/\langle t\rangle$. However, the traveltime is equal to φ/ω. Therefore, the relative standard deviations of the traveltimes for several travel-distances yields the theoretically obtained $1/\sqrt{L}$ dependency (3.38), which is also shown in Figure (3.2).

It is interesting to note that the process of self-averaging is not only restricted to the weak wave field fluctuation range. In the described numerical experiment strong fluctuations (the incoherent parts are of the order of the coherent part) occur at travel-distances larger than $\approx 400m$. Figures (3.1) - (3.4) clearly show, however, that the self-averaging is still valid in the range of the transition from weak to strong wave field fluctuations. Figure (3.5) displays the numerically determined $\sigma_\alpha/\alpha(\omega_0)$ as a function of L for 6 simulations with varying correlation lengths and standard deviations. In full agreement with equation (3.36) we observe the decrease of σ_α/α with L behaves like $1/\sqrt{L}$ and is stronger for larger medium's fluctuations and smaller correlation lengths. Also we observe the decrease of the relative standard deviation of the traveltime fluctuations with increasing travel-distance (Figure 3.6) according to equation (3.38). Note that the decrease of σ_φ/φ with travel-distance becomes weaker if the medium fluctuations increase. The opposite behavior can be observed for σ_α/α.

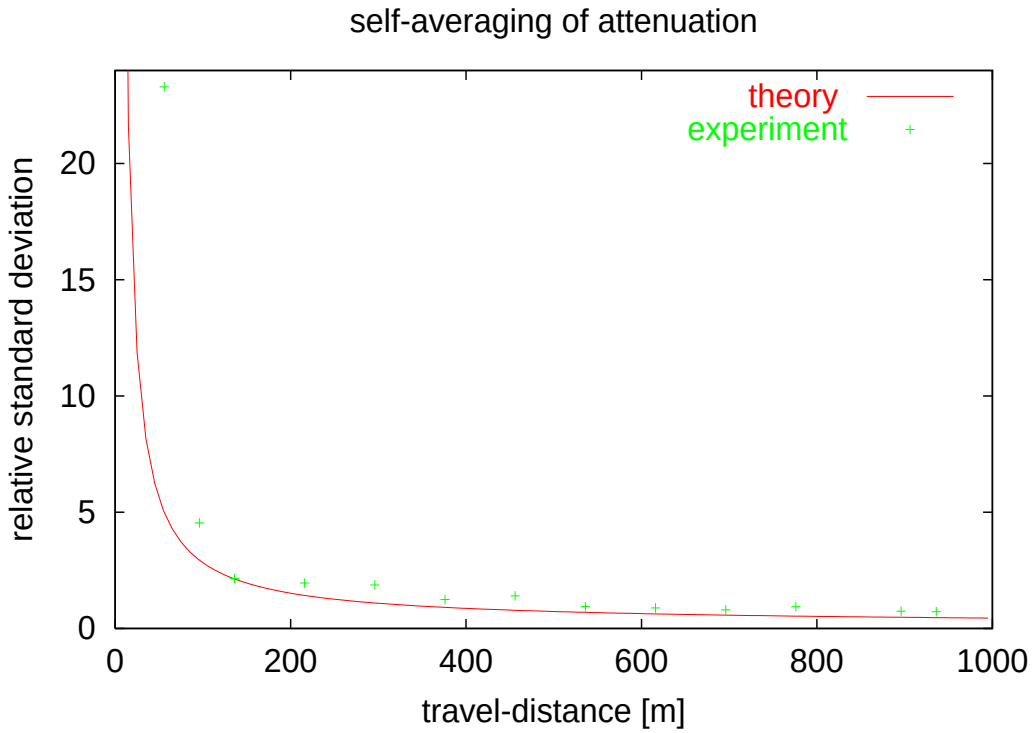

Figure 3.1: The relative standard deviations of the attenuation coefficient of an initially plane wave for a 2-D exponentially correlated random medium. The solid line corresponds to the theoretical result given by equation (3.36). The corresponding numerical results (FD modeling) are shown by the crosses. The exponential (elastic) random medium realization is characterized by $v_P = 3000m/s$, $\sigma_n = 0.15$ and $a = 40m$. The S-wave velocity ($v_S = 1850m/s$) and the density ($\rho = 2.5g/cm^3$) are constants.

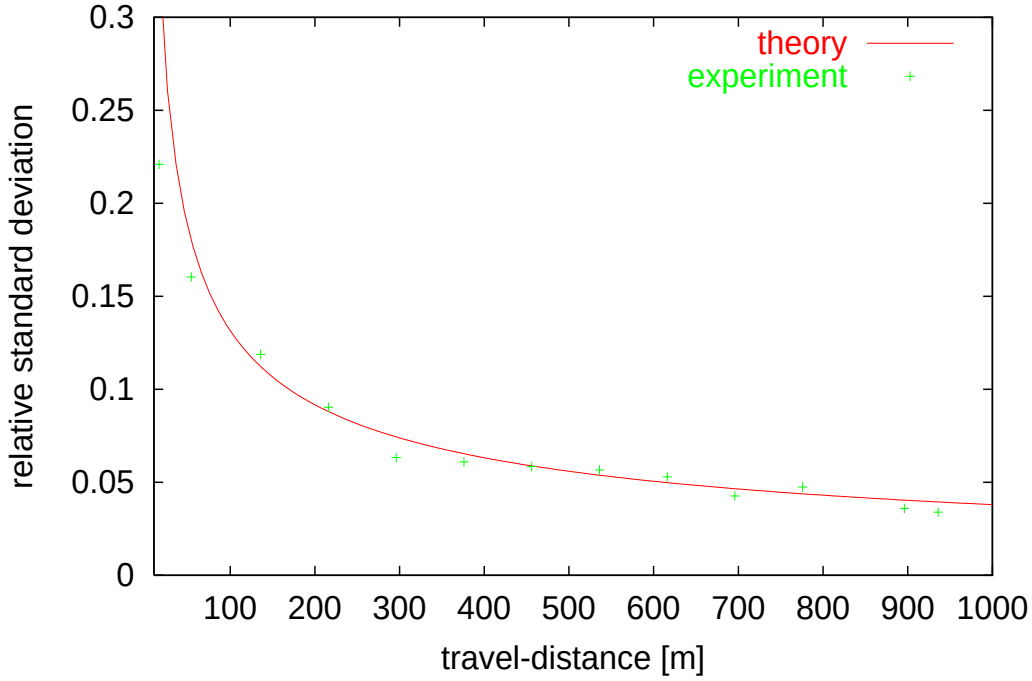

Figure 3.2: The relative standard deviations of the phase increment for a 2-D exponentially correlated random medium. The solid line corresponds to the theoretical result given by equation (3.38), whereas the crosses denote the numerical results from FD modeling. The parameters of the numerical model are the same as in Figure (3.1).

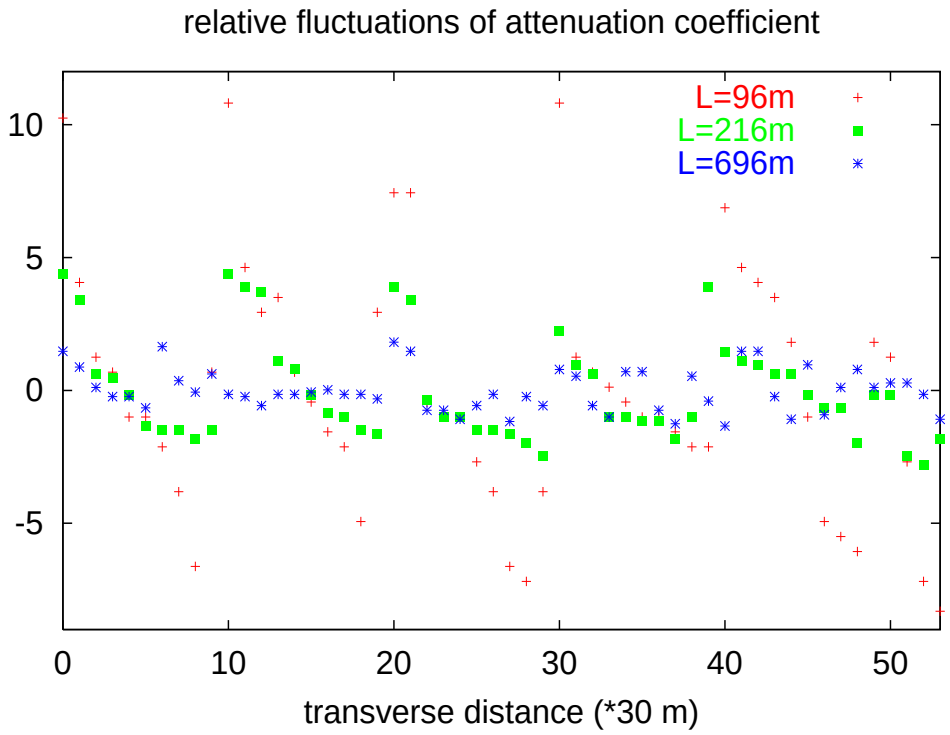

Figure 3.3: Relative fluctuations of the attenuation coefficient inverted from 54 geophones along a receiver-line for three different depths. For increasing travel-distances the relative fluctuations become smaller. The parameters of the numerical model are the same as in Figure (3.1).

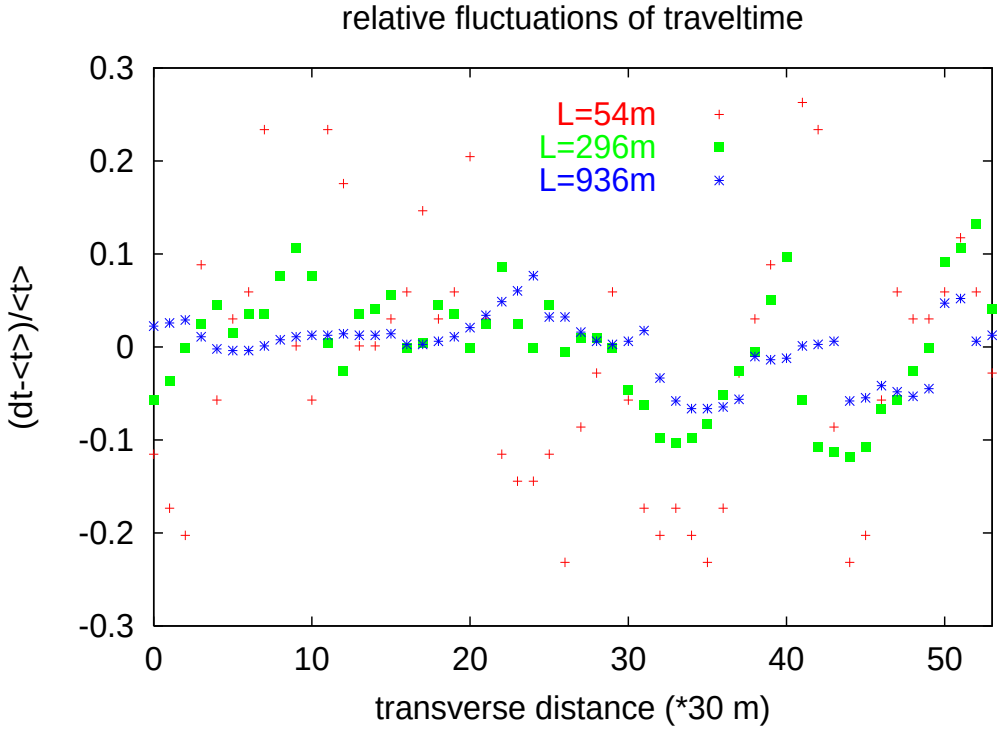

Figure 3.4: Relative fluctuations of the traveltime recorded at 54 geophones along a receiver-line for three different depths. For increasing travel-distances the relative fluctuations become smaller. The parameters of the numerical model are the same as in Figure (3.1).

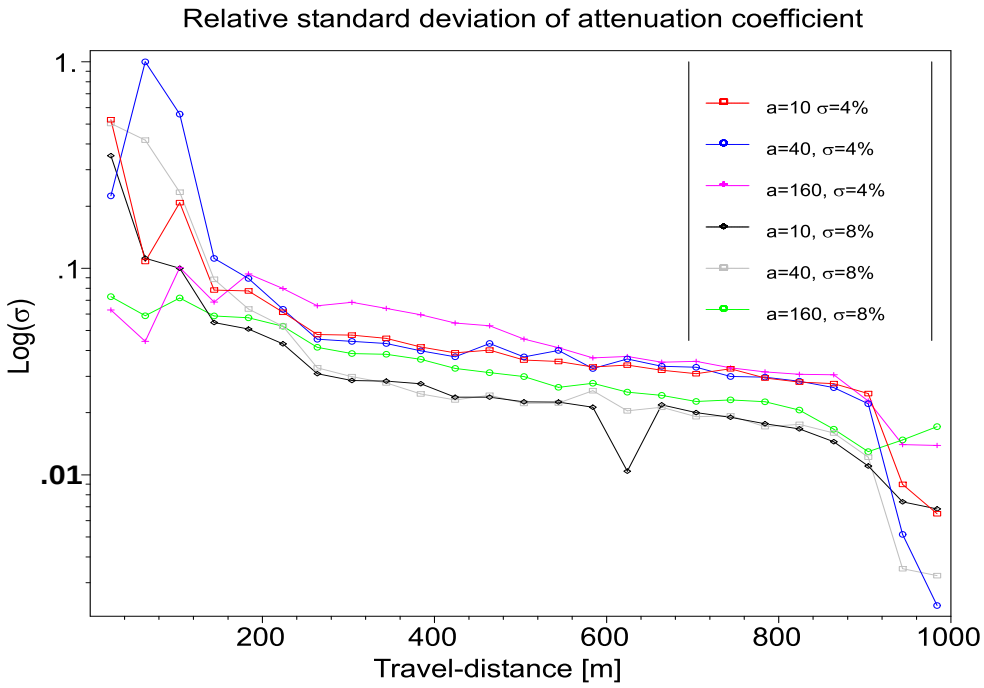

Figure 3.5: The relative standard deviations of the attenuation coefficient for a 2-D exponentially correlated random medium evaluated for the numerical experiments described in detail in section (2.2). For all investigated ratios of λ/a and standard deviations we can observe a decrease of the relative standard deviations with increasing travel-distances (note that the ordinate axis is logarithmically spaced). In agreement with equation (3.36), the relative standard deviations of the attenuation coefficient decrease faster with increasing standard deviation of the velocity fluctuations and with decreasing correlation lengths.

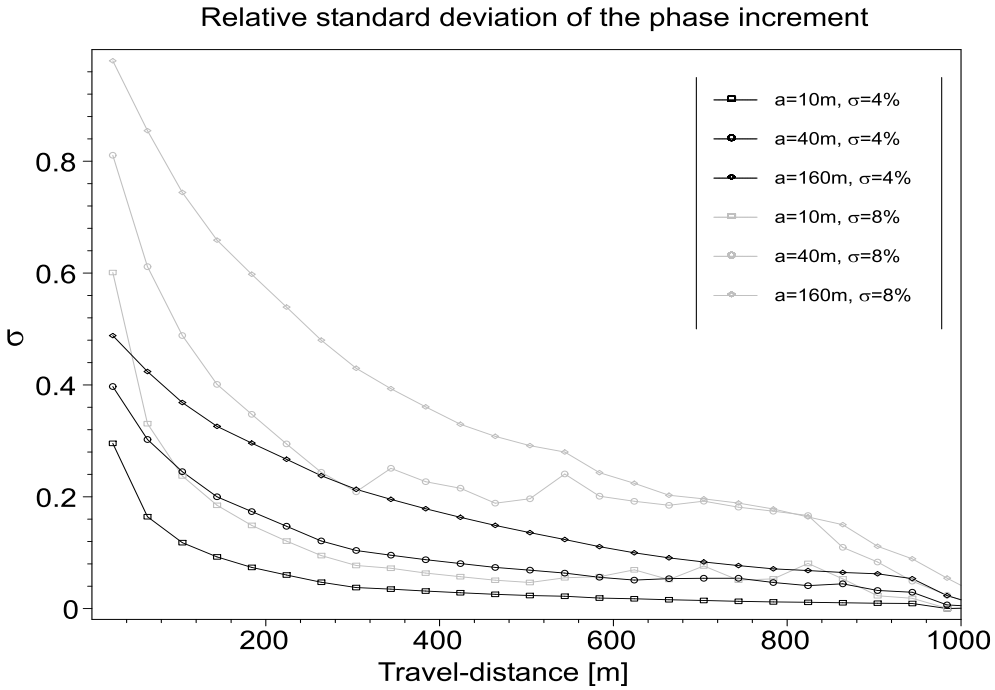

Figure 3.6: The relative standard deviations of the phase increment for a 2-D exponentially correlated random medium.

3.5.2 Typical (most probable) wave field realizations

As already mentioned, within the validity range of the Rytov approximation (that implies for finite travel-distances) only a partial self-averaging can be reached. That is to say the probability densities of the wave field attributes have not yet converged to a δ-function what would indicate that the quantities are not any more random. Therefore, it is expedient to look for the probability density of the logarithmic wave field attributes and to introduce the concept of typical realizations of a stochastic process. Typical realizations are defined to be close to the most probable realization which is defined by the maximum of the probability density function (Lifshits et al., 1988, pp. 373). Now, the partial self-averaging means that we deal with ballistic wave field realizations that are most likely to occur and therefore are typical (or equivalently most probable) realizations.

The self-averaging property of a quantity makes it possible to characterize a specific realization in terms of the mean value of this quantity. In the contrary, for non-self-averaged quantities, the mean value is not adequate to attach a physical meaning to a specific realization (Gredeskul and Freilikher, 1990). The reason for this behavior is that such mean values are dominated by representative realizations. Representative realizations are those realizations of a quantity that are in the neighborhood of the average value of this quantity (see for illustration Figure 3.7).

It can be theoretically and experimentally shown that χ and ϕ are normally distributed random variables (see chapter (2.5) in Rytov et al. (1989) and section 2.3). If χ is described by the probability density $p(\chi) = \frac{1}{\sigma\sqrt{2\pi}} e^{-(\chi-\eta)^2/2\sigma^2}$ (where η and σ are the mean and standard deviation, respectively), then we might expect that the Rytov transformation yields log-normal distributed wave field amplitudes. Indeed, in section (2.3.1) we numerically confirmed the log-normal probability density of the wave field amplitudes $p(A) = \frac{1}{\sigma A\sqrt{2\pi}} e^{-(\ln A-\eta)^2/2\sigma^2}$.

With the above criterion, it is possible to find the typical realizations from numerical experiments by constructing the probability density functions and to compare them with the discussed wave field attributes. The identification of typical ballistic seismograms is explained in section (3.8.1).

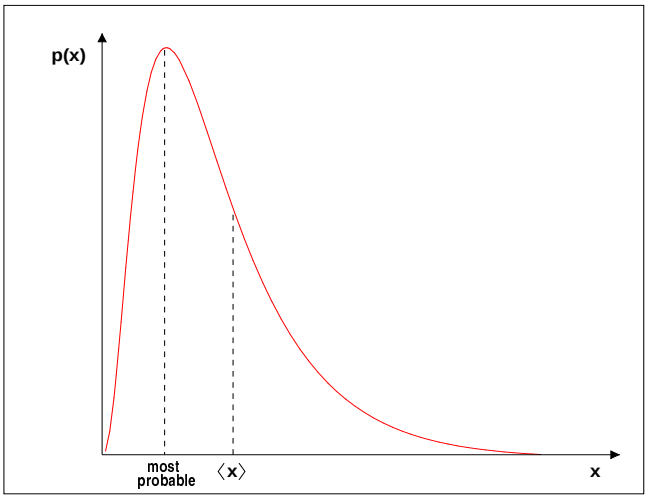

Figure 3.7: The PDF of a random variable x and its corresponding mean and most probable value. For PDF's with large skewness, the mean value is not expedient to characterize the random process.

Amplitudes and waveforms are quite variable along the wavefront in 2-D and 3-D random media (see e.g. the wave field snapshots in Figure (2.8)). This is of course not the case

in 1-D media. There is no need to look for typical realizations of seismograms since only one waveform is observable in a single realization of the random medium. Shapiro and Hubral (1999) demonstrated the self-averaging of the attenuation coefficient in the frequency domain. Moreover, in 1-D media the self-averaging phenomenon leads to a pulse stabilization for larger travel-distances (e.g. Lewicki, 1994, and Lewicki et al., 1994). That means relative to a random traveltime, the form of a propagating pulse converges to a non-random waveform.

3.6 Attenuation and phase velocity dispersion

Attenuation and dispersion of wave fields are fundamental quantities in rock characterization. Especially the derived logarithmic wave field attributes enable to describe the frequency behavior of the the scattering attenuation coefficient and that of the phase velocity. These results can be useful for geophysical upscaling problems as encountered when comparing lab and field measurements (Mukerji et al., 1995).

3.6.1 Plane waves

Scattering attenuation

As shown in section (3.4), the attenuation coefficient is in 3-D given by

$$\begin{aligned}
\alpha^{3D} &= \alpha_R(\omega) + \alpha_B(\omega) \\
&= 2\pi^2 k^2 \int_0^\infty d\kappa\, \kappa\, \Phi^{3D}(\kappa) \left[1 - \frac{\sin(\kappa^2 L/k)}{\kappa^2 L/k}\right] - 2\pi^2 k^2 \int_{2k}^\infty d\kappa\, \kappa\, \Phi^{3D}(\kappa) \\
&= 2\pi^2 k^2 \int_0^\infty d\kappa\, \kappa\, \Phi^{3D}(\kappa) \left[H(\kappa - 2k) - \frac{\sin(\kappa^2 L/k)}{\kappa^2 L/k}\right], \qquad (3.39)
\end{aligned}$$

and analogously in 2-D random media

$$\alpha^{2D} = 2\pi k^2 \int_0^\infty d\kappa\, \Phi^{3D}(\kappa) \left[H(\kappa - 2k) - \frac{\sin(\kappa^2 L/k)}{\kappa^2 L/k}\right], \qquad (3.40)$$

where H is the Heaviside step function. Instead of plotting the attenuation coefficient, we show the frequency dependence of the reciprocal quality factor

$$Q^{-1} = 2\alpha/k \qquad (3.41)$$

in Figure (3.8). The lower part of Figure (3.8) depicts the the reciprocal quality factor as a function of ka in a 3-D Gaussian correlated random medium for various L/a. The upper part of Figure (3.8) shows the reciprocal quality factor for waves propagating in 2-D, 3-D exponentially and Gaussian correlated random media based on the approximation (3.29). In the same Figure $1/Q$ for 1-D random media is displayed. We used the corresponding expressions of the ODA theory of Shapiro and Hubral (formulas 4.18). All curves are normalized by $\sqrt{\pi}\sigma_n^2$. Whereas in 1-D the attenuation is independent of the parameter L/a, in 2-D and 3-D we observe a dependence in L/a. Especially in Gaussian random media the maximum attenuation occurs roughly at $ka = L/a$ which corresponds to the so-called Fresnel length. Note that in 2-D and 3-D, attenuation in Gaussian random media is slightly larger than in exponentially correlated ones for $ka < 1$. This relation becomes reversed for $ka > 1$.

In the low-frequency limit, we can approximate the spectral filter function –defined in appendix B – in equation (B.1) by 1. Then equation (3.39) can be written as

$$\begin{aligned}\alpha_{\text{low}}^{3D} &= 2\pi^2 k^2 \int_0^\infty d\kappa\, \kappa\, \Phi^{3D}(\kappa) - 2\pi^2 k^2 \int_{2k}^\infty d\kappa\, \kappa\, \Phi^{3D}(\kappa) \\ &= 2\pi^2 k^2 \int_0^{2k} d\kappa\, \kappa\, \Phi^{3D}(\kappa) \quad . \end{aligned} \tag{3.42}$$

Analogously we obtain in 2-D media:

$$\alpha_{\text{low}}^{2D} = 2\pi k^2 \int_0^{2k} d\kappa\, \Phi^{2D}(\kappa) \quad . \tag{3.43}$$

Equations (3.42)-(3.43) coincide with the mean field attenuation coefficient as derived by various authors (Rytov et al., 1989, Shapiro and Kneib, 1993). Therefore, there is a smooth transition from the attenuation derived from the Rytov approximation towards the mean field attenuation. This fact explains the equivalence between the low-frequency Rytov attenuation and the mean field attenuation in the case of large inhomogeneities (see equations (32)-(33) and (A2-16)-(A2-17) of Shapiro and Kneib). Inserting for example the fluctuation spectrum for 3-D exponential media $\Phi^{3D}(\kappa) = \frac{\sigma_n^2 a^3}{\pi^2(1+\kappa^2 a^2)^2}$, we get

$$\alpha_{\text{low}}^{3D} = 4\sigma_n^2 \frac{k^4 a^3}{1+4k^2a^2} \approx 4\sigma_n^2 a^3 k^4 \quad , \tag{3.44}$$

whereas for 3-D Gaussian random media with $\Phi^{3D}(\kappa) = \frac{\sigma_n^2 a^3}{8\pi^{3/2}} e^{-\kappa^2 a^2/4}$ we get

$$\alpha_{\text{low}}^{3D} = \frac{\sqrt{\pi}\sigma_n^2}{2} k^2 a \left(1 - e^{-k^2a^2}\right) \approx \frac{\sqrt{\pi}\sigma_n^2}{2} k^4 a^3 \quad . \tag{3.45}$$

yielding the expected Rayleigh frequency dependency. Note that equations (3.42), (3.43) are only valid provided that the inequality (3.34) holds.

The high-frequency limit of the attenuation coefficient can be derived by the following consideration. Applying a Taylor series expansion of the spectral filter function for small argument L/k (or equivalently $D \ll 1$) yields

$$\left(1 - \frac{\sin(\kappa^2 L/k)}{\kappa^2 L/k}\right) = \frac{1}{6}\left(\frac{\kappa^2 L}{k}\right)^2 + \mathcal{O}\left(\left(\frac{\kappa^2 L}{k}\right)^4\right) . \tag{3.46}$$

This yields the frequency independent equation:

$$\sigma_{\chi\chi}^2 = \frac{\pi^2}{3} L^2 \int_0^\infty d\kappa\, \kappa^5 \Phi^{3D}(\kappa) \tag{3.47}$$

and consequently

$$\alpha_{\text{high}}^{3D} = \frac{\pi^2}{3} L^3 \int_0^\infty d\kappa\, \kappa^5 \Phi^{3D}(\kappa) \tag{3.48}$$

(see e.g. equations (30) and (31) of Shapiro and Kneib (1993) for the expression in 2-D). Therefore, the attenuation tends for large ka towards the constant $\alpha_{\text{high}}^{3D} = \frac{8\sqrt{\pi}}{3}\sigma_n^2 \frac{L^2}{a^3}$ in 3-D Gaussian media. This corresponds to the log-amplitude variance divided by the travel-distance in the geometrical optic limit. For exponentially correlated fluctuations in 2-D and 3-D, the attenuation increases without limit for increasing ka (see also Figure (3.8)).

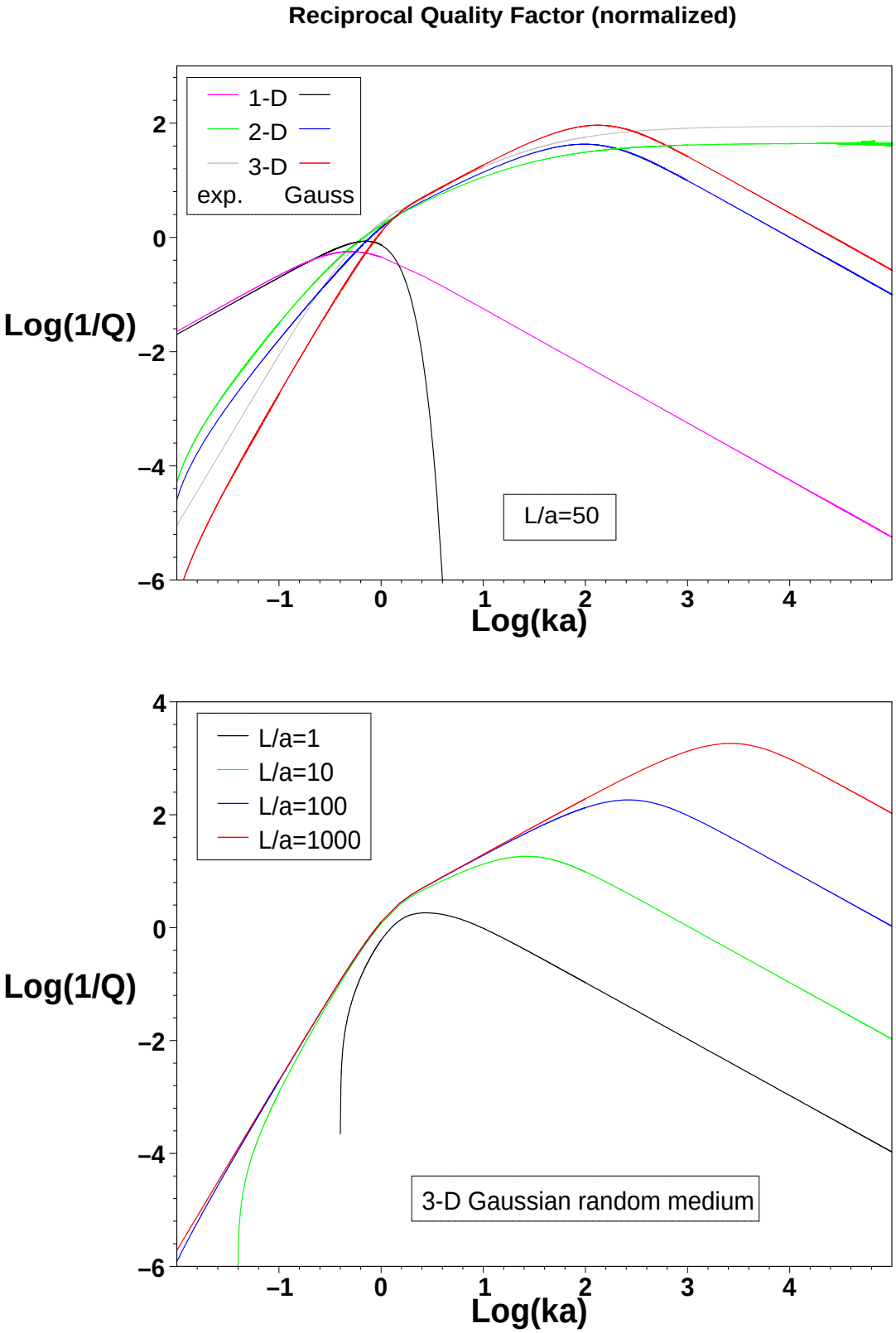

Figure 3.8: The reciprocal quality factor $1/Q = 2\alpha/k$ corresponding to a plane wave as a function of ka for Gaussian and exponentially correlated random media in 1-D, 2-D and 3-D (upper plot). The L/a dependency of the reciprocal quality factor is shown for a 3-D Gaussian random medium in the lower plot. All curves are normalized by $\sqrt{\pi}\sigma_n^2$.

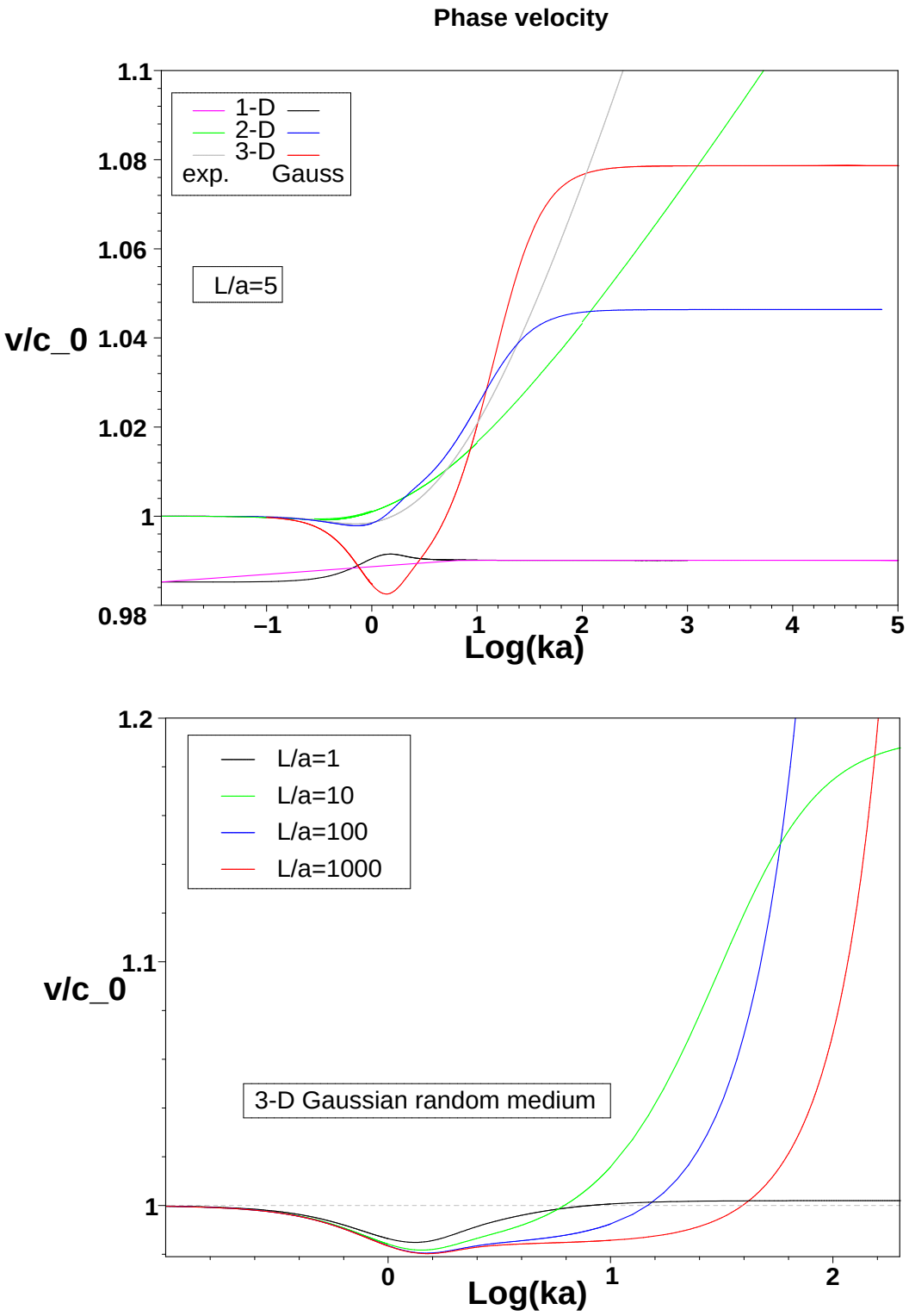

Figure 3.9: Phase velocity normalized by the background velocity c_0 as a function of ka for Gaussian and exponentially correlated random media in 1-D, 2-D and 3-D (upper plot). The dependence on the parameter L/a in a 3-D Gaussian correlated medium is shown in the lower plot.

Phase velocity

The phase velocity can be expressed in terms of the averaged phase:

$$v = \frac{\omega L}{\phi_0 + \langle\phi\rangle} = c_0 \frac{ka}{ka + \frac{a}{L}\langle\phi\rangle} \quad . \tag{3.49}$$

The phase fluctuations cause traveltime fluctuations when considering wave field registrations at points of surfaces parallel to the wavefront of the initial plane wave. This results in the so-called velocity shift which can be physically explained by the fast-path effect and is characteristic for multiple scattering processes (see e.g. Müller et al., 1992, Samuelides, 1998, and Shapiro et al.,1996b, for a frequency-dependent description of this effect). Figure (3.9) displays the phase velocity as a function of the dimensionless wavenumber ka for waves propagating in 1-D, 2-D and 3-D Gaussian correlated random media. It is this path effect which causes the velocity increase from low to high frequencies to be much larger in 2-D and 3-D than in one dimensional media. Note that in 1-D there is no travel-distance dependency. The lower part of Figure (3.9) displays the phase velocity dependence on the parameter L/a.

Let us discuss the low-frequency behavior of the phase velocity. For $ka < 1$ the contribution of $\sigma^2_{\chi\phi}$ (equation (B.2)) becomes neglegebly small and the phase is determined by the coherent phase ϕ_c. in the limit $ka \to 0$ one obtains $v_{2D,3D} = c_0$. This is in fact the effective media limit (see e.g. Mukerji et al., 1995). For infinitely large ka the phase velocity tends towards a constant in the case of Gaussian random media, whereas it increases without limit in exponential random media. Note that at the same time the attenuation coefficient is also increasing to infinity.

3.6.2 Spherical waves

Whereas the previous sections have been concerned with plane wave attenuation and dispersion, we turn now the attention to the attenuation of waves radiating from a point source. Equations (3.17), (3.18) describing the logarithmic wave field attributes are also valid for spherical wave propagation. This is not true for equations (3.29) which are based on the causality principle. Nevertheless, even in equation (3.18) the coherent phase is obtained for a point source in a random medium. We approximate the attenuation of spherical waves by replacing the log-amplitude variance of plane waves in equation (3.29) by its respective counterpart for spherical waves (see Ishimaru (1978), chapter 18 and appendix B for explicit expressions).

Then, the attenuation coefficient in 3-D random media reads

$$\begin{aligned} \alpha^{\text{point}} \quad \approx \quad & 2\pi^2 k^2 \int_0^\infty d\kappa\, \kappa\, \Phi^{3D}(\kappa) \\ & \left[H(\kappa - 2k) - \frac{\cos(\pi/2A^2)\, C(A) + \sin(\pi/2A^2)\, S(A)}{A} \right] . \end{aligned} \tag{3.50}$$

In equation (3.50) we use $A = \sqrt{\frac{\kappa^2 L}{2\pi k}}$. The functions C and S denote the Fresnel cosine and sine integrals, respectively. They are defined in equation (B.8). The attenuation coefficient

in 2-D random media can be obtained from the above formula by dividing by π and skipping the κ inside the integral. The resulting reciprocal quality factors are shown in Figures (3.10) and (3.11) for different fluctuation spectra in 2-D and 3-D random media.

It is interesting to consider the high-frequency limit of equation (3.50). Note that the Fresnel integrals for small arguments can be approximated as follows: $C(A) \approx A$ and $S(A) \approx \pi/6\, A^3$ (see Born and Wolf, 1999). Then, the term in rectangular brackets of equation (3.50) becomes

$$1 - \left[\cos\left(\frac{\pi}{2}A^2\right) + \frac{\pi}{6}A^2 \sin\left(\frac{\pi}{2}A^2\right)\right] . \tag{3.51}$$

Expanding also the sine and cosine functions, equation (3.51) simplifies to $\frac{\pi^2}{24}A^4$ and the attenuation coefficient is

$$\alpha_{\text{high}}^{\text{point}} = \frac{\pi^2}{48} L^3 \int_0^\infty d\kappa\, \kappa^5\, \Phi(\kappa) . \tag{3.52}$$

Comparing this with its plane wave analogon (3.48), one obtains

$$\alpha_{\text{high}}^{\text{plane}} = 16\, \alpha_{\text{high}}^{\text{point}} . \tag{3.53}$$

That is to say plane waves are 16 times stronger attenuated than waves excited by a point source (in the high-frequency limit). Intuitively it is clear that plane waves are stronger attenuated since neighboring increments of a plane wave front, scattered in different directions when impinging on a random medium, have more possibilities to interfere and yield larger (log)amplitude fluctuations than for a spherical wave front. But these log-amplitude fluctuations are in our approximation related to the scattering attenuation (see again equation (3.17)). Rytov et al. (1989) explain this behavior in terms of the lens effect. They show by a ray theoretical consideration that the log-amplitude variance ($\sigma_{\chi\chi}^2$) for plane waves is 10 times larger than that for spherical waves.

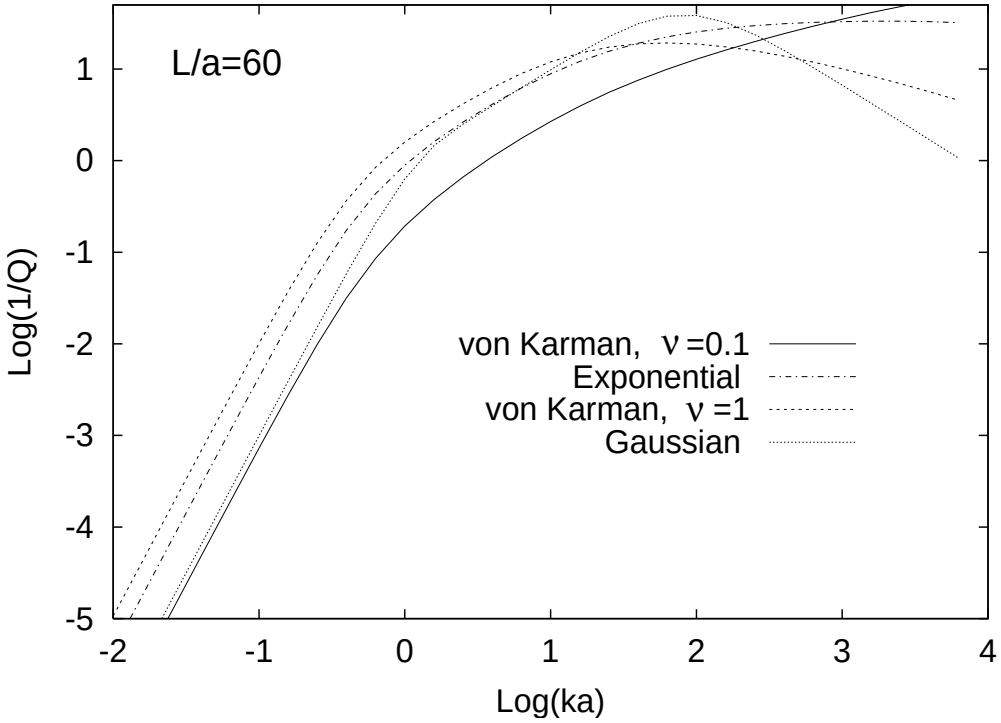

Figure 3.10: The reciprocal quality factor for a spherical wave as a function of ka for 3-D random media using different fluctuation spectra. The von Kármán fluctuation spectrum is additionally characterized by the Hurst number ν.

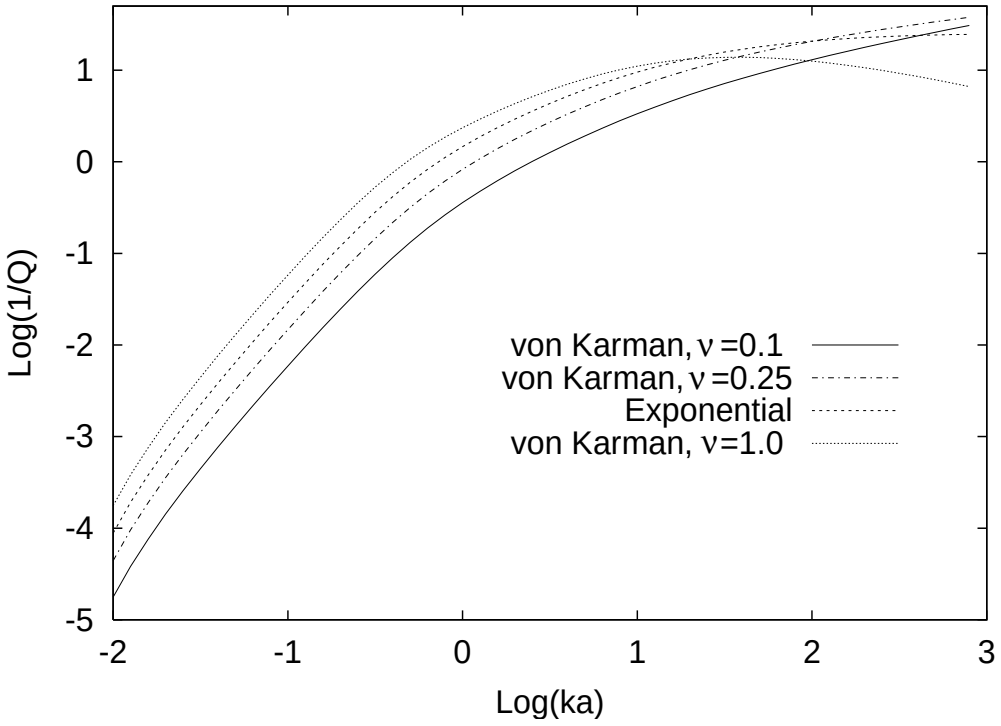

Figure 3.11: The reciprocal quality factor for a spherical wave as a function of ka for 2-D random media. The normalized travel-distance is $L/a = 50$.

3.6.3 Relation to other scattering attenuation models

The importance of seismic wave scattering was early recognized as an important aspect of seismic data analysis and rock characterization (for an overview we refer to Sato and Fehler, 1998, and the references therein). In this section we show how the above presented scattering attenuation model is related to scattering attenuation of the mean field and traveltime-corrected mean field obtained in the Born approximation.

To do so, we examine the scattering attenuation estimate given in the traveltime-corrected Born approximation (see equation 5.20 in Sato and Fehler, 1998)

$$ {}^{TSc}Q^{-1} = \frac{k^3}{2\pi} \int_{\vartheta_c}^{\pi} \Phi\left(2k \sin\left[\frac{\vartheta}{2}\right]\right) \sin(\vartheta)\, d\vartheta\,, \tag{3.54} $$

where ϑ_c denotes the scattering angle. Theoretical and numerical considerations suggest $\vartheta_c \approx 29^o$. Note that equation (3.54) refers to a traveltime-corrected averaged field in the sense that all waveforms have to be aligned to a certain reference time and then summed up. After some straightforward calculations we can express ${}^{TSc}Q^{-1}$ as

$$ {}^{TSc}Q^{-1} = \frac{k}{2\pi} \int_0^{2k} d\kappa\, \kappa\, \Phi(\kappa) - \int_0^{2k \sin\left[\frac{\vartheta_c}{2}\right]} d\kappa\, \kappa\, \Phi(\kappa)\,. \tag{3.55} $$

From the latter equation it is easy to see how ${}^{TSc}Q^{-1}$ is related to the mean field attenuation: For $\vartheta_c = 0$ the second integral vanishes and the first term corresponds to the mean field attenuation (see e.g. equation (A2-17) in Shapiro and Kneib, 1993). Exactly the same expression can be observed in equation (3.39) by considering only the first term and reducing the integration limits by virtue of the Heaviside step function. By comparing the remaining terms in equations (3.39) and (3.55), it is possible to derive in the long travel-distance limit (Fraunhofer approximation) a relationship between the scattering angle (needed for ${}^{TSc}Q^{-1}$) and the travel-distance which enters into equation (3.39):

$$ \vartheta_c \approx 2 \arcsin\left[\sqrt{\frac{\pi}{8Lk}}\right]\,. \tag{3.56} $$

Equations (3.54)-(3.56) show that both models of scattering attenuation based on the single scattering approximation can be derived from the more general equation (3.39). A formulation of the traveltime-corrected mean field based on the wave field attributes (3.17) and (3.18) is given in section (3.8.2).

3.7 Green's function for the primary wave field

3.7.1 Acoustic media

Now, we show how finite-bandwidth pulses evolve in time when propagating in random media. In order to construct the Green's function we have to combine the results for the ensemble-averaged log-amplitude and phase fluctuations obtained in equations (3.29) and (3.30). Finally, by integration over the whole range of frequencies (an inverse Fourier transform) we obtain the time-dependent transmission response due to the initial plane wave:

$$\begin{aligned} G(t,L) &= \frac{1}{2\pi}\int_{-\infty}^{\infty} d\omega\, e^{iK(\omega,L)L} e^{-i\omega t} \\ &= \frac{1}{2\pi}\int_{-\infty}^{\infty} d\omega\, e^{-\alpha(\omega,L)L + i\varphi(\omega,L)L} e^{-i\omega t}\,. \end{aligned} \tag{3.57}$$

That is what we call the Green's function for random media; it is a real function since its Fourier transform consists out of an even real part and an odd imaginary part (see also equations (B.1)-(B.9)). In Figures (3.12) and (3.13), the real and imaginary part of $\exp(iKL)$ are displayed as a function of frequency for several travel-distances L (the narrower the curve, the larger the travel-distance). The validity range of the Green's function is defined by the approximations used and has been already discussed in section (3.4.2).

In Figure (3.14) we depict this Green's function based on the wave field attributes (3.29) - (3.30) for several travel distances in an exponentially correlated 2-D random medium. We can clearly observe the decrease of the transmission response for increasing travel-distances. This is only due to scattering attenuation. We observe also the broadening of the pulses. In Figure (3.15) the Green's functions corresponding to Gaussian and exponentially correlated random media are compared.

In general, equation (3.57) can be efficiently evaluated using a FFT-routine.
It is now possible to describe seismic pulses as

$$u(t,L) = \frac{1}{2\pi}\int_{-\infty}^{\infty} d\omega\, U_0(\omega) e^{i(KL-\omega t)} \tag{3.58}$$

$$= G(t,L) * u_0(t) \quad , \tag{3.59}$$

where $U_0(\omega)$ is the Fourier transform of the input signal $u_0(t)$ and the asterisk stands for convolution in time. Due to the use of averaged wave field attributes $\langle\chi\rangle$ and $\langle\phi\rangle$ (instead of χ and ϕ) obtained in the Rytov approximation, equation (3.58) gives a description of the main part of the transmitted pulse around the primary arrivals. We will confirm this by numerical simulations in section 3.8. Later arrivals, i.e. the coda are not predicted within this approximation.

3.7.2 Gaussian pulse approximation

In order to obtain explicit analytical results for the Green's function in the time domain (that is to evaluate the integral in equation (3.57)), we have to introduce some simplifications. To do so, we study the behavior of equation (B.1) in the Fraunhofer approximation. The latter is characterized by a large wave parameter $D \gg 1$ so that the spectral filter functions in equations (B.1)-(B.3) become unity and the mean of phase fluctuations can be neglected. The Fraunhofer approximation becomes valid for large travel-distance L. From the behavior of scattering attenuation, it turns out that for large travel-distances only the low-frequency components of the transmitted pulse survive. Thus, with increasing L not only L/a but also $(ka)^{-1}$ effectively increases. Therefore, equation (3.57) can be reduced to:

$$G_{\mathrm{apr}}(t,L) = \frac{1}{2\pi} \int_{-\infty}^{\infty} d\omega \, e^{-L\alpha_{\mathrm{low}}} e^{i(kL-\omega t)} \quad , \tag{3.60}$$

where α_{low} is given by equation (3.42). To account for $D \gg 1$ or equivalently $2L/a^2 \gg k$ we replace the upper integration limit in (3.42) by $4L/a^2$ without incurring error. Evaluating then the integral in (3.60) yields a Gaussian pulse (in 2-D as well as in 3-D).

$$G_{\mathrm{apr}}(t,L) = \sqrt{\frac{A}{L}} e^{-\frac{\pi A}{L}(t-L/c_0)^2} \tag{3.61}$$

with $A = c_0^2/(4\pi\hat{\alpha})$, where $\hat{\alpha} = 2\pi^2 \int_0^{4L/a^2} d\kappa \, \kappa \, \Phi^{3D}(\kappa)$ in 3-D (and $\hat{\alpha} = 2\pi \int_0^{4L/a^2} d\kappa \, \Phi^{2D}(\kappa)$ in 2-D).

It is interesting to note that the $1/\sqrt{L}$ dependency of the pulse in 2-D and 3-D is also obtained for 1-D random media (compare with equation (7.8) in Shapiro and Hubral, 1999). In Figure (3.16) we see the pulse evolution in a 3-D Gaussian random medium using the Gaussian pulse approximation (3.61) (gray curves) and the Green's function (3.57) (black curves). Note that the same result can be obtained by considering the random medium as a stack of statistically identical random media and then evaluating the multiple product of Green's functions. The evaluation of products of functions is based on the central limit theorem (Uscinski, 1982).

Interestingly, the envelope of these Gaussian pulses is simply given by

$$E(t) = \sqrt{\frac{A}{\tilde{L}}} \quad e^{-\frac{\pi A}{\tilde{L}}(t-\tilde{L}/c_0)^2} \quad , \tag{3.62}$$

where $\tilde{L} = \frac{c_0}{4A}(\sqrt{c_0^2 + 16A^2t^2} - c_0)$, which itself is a Gaussian function in time. This Gaussian envelope can be clearly observed in the numerical experiments. In Fig. (2.11) the space-curve connecting the maxima of the PDF of amplitudes corresponds to equation (3.62). In Fig. (3.16) we see the pulse evolution in a 3-D Gaussian random medium and the corresponding envelope from equation (3.62).

3.7.3 Elastic media

A wave field description in elastic media should be based on the elastodynamic wave equation. In appendix E we briefly discuss the generalizations of the Rytov as well as the Bourret approximations to elastic media. Under the assumption of weak wave field fluctuations, the propagation of elastic waves shows practically the same behavior as acoustic waves (Aki and Richards, 1980).

The Rytov approximation for elastic P- and S-waves yields for the complex exponent Ψ in 2-D and 3-D random media the following equation:

$$\Psi_{P,S}^{2D,3D} = 2\begin{pmatrix}\alpha^2\\ \beta^2\end{pmatrix}\int n_v(\mathbf{r}')\frac{U_0(\mathbf{r}')}{U_0(\mathbf{r})}\,G^{2D,3D}(\mathbf{r}-\mathbf{r}')\,d\mathbf{r}' \quad , \tag{3.63}$$

where $G^{2D,3D}$ is the acoustic Green's function in 2-D/3-D and α, β are the P- and S-wave numbers, respectively. n_v denotes the velocity fluctuations expressed as a function of the fluctuations of the Lamé parameters and density according to equation (E.11). This is exactly equation (17-19) of Ishimaru (1978) which states the first Rytov approximation for acoustic media and consequently the log-amplitude and log-amplitude phase (cross-) variances can be computed in the same way resulting in the expressions of appendix B.1. Gold et al. (2000) applied the Bourret approximation in the Dyson equation in order to obtain the coherent Green's function in isotropic elastic random media. From this consideration the coherent phase ϕ_c is obtained and can be used for equation (3.18). That means the wave field approximation based on equations (3.17) and (3.18) can be used in the elastic case. Moreover, we assume also that the relations (3.29) and (3.30) hold. Due to the complexity of the wave field attributes, a direct application of the Kramers-Kronig relations is not possible. However, this assumption seems reasonable at least in the light of our numerical calculations.

Note that the validity range of the elastic Green's function for the primary wave field is more difficult to state because of conversion scattering (see section 2.1.4). The forward scattering assumption used in order to derive equation (3.63) is equivalent to the neglect of any conversion. However, the elastic Bourret approximation is not based on this assumption. So, the hybrid character of the wave field approximation based on equations (3.29) and (3.30) accounts for a part of the conversion scattering. A rigorous treatment is not amenable within the extended ODA approach.

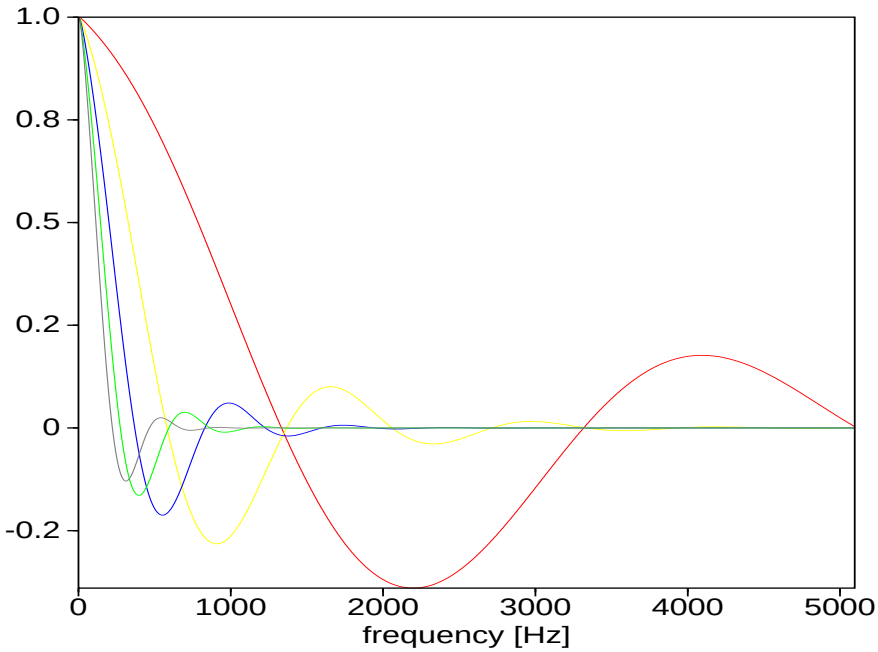

Figure 3.12: Real part of the Green's function ($e^{-\alpha L}\cos(\varphi L)$) in the frequency domain for positive frequencies. Note that the real part is an even function.

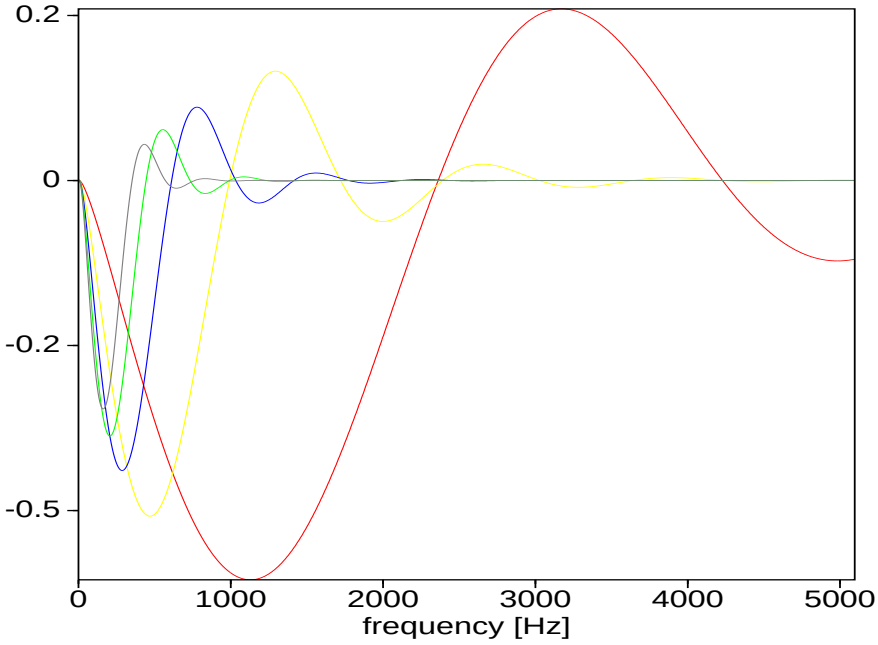

Figure 3.13: Imaginary part of the Green's function ($e^{-\alpha L}\sin(\varphi L)$) in the frequency domain for positive frequencies. Note that the imaginary part is an odd function.

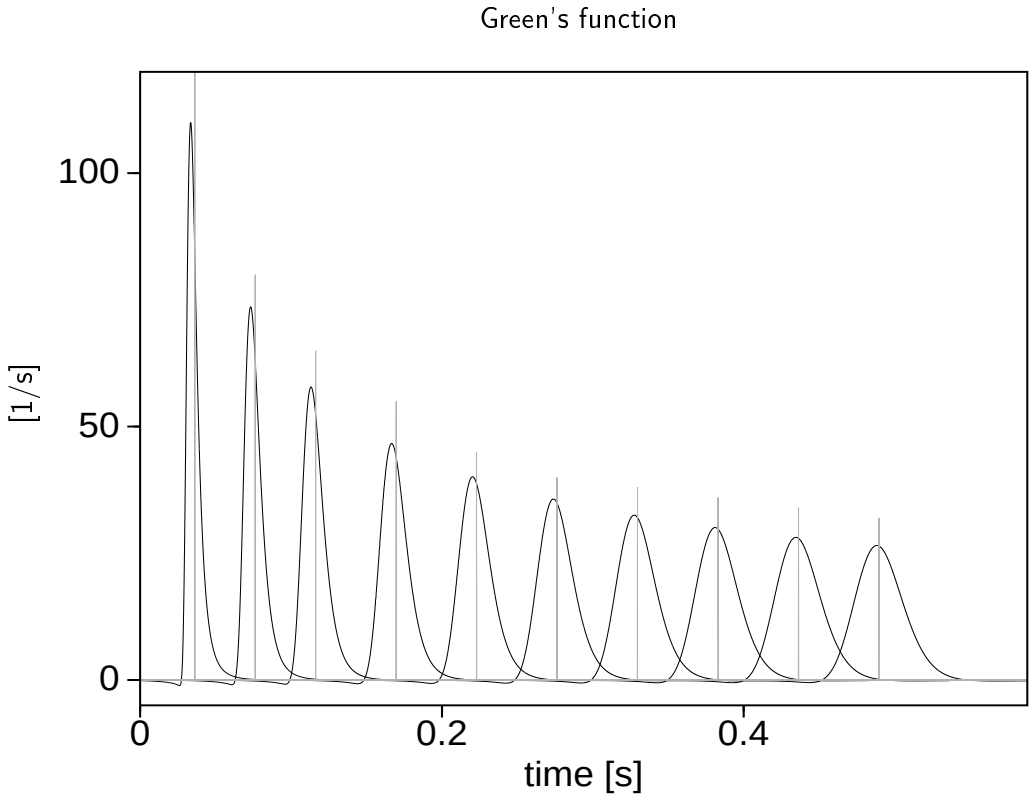

Figure 3.14: Green's function based on the wave field attributes (3.29)-(3.30) (black curves) for several travel-distances. The pulses from left to right denote the transmission response of the exponential random medium (the standard deviation of the velocity fluctuations is 15%, the correlation length is $40m$) due to a δ-pulse excitation for the travel-distances $L =$ 256, 376, 496, 656, 816, 976, 1136, 1296, 1456, 1616 m, respectively. For increasing travel-distances the amplitudes decrease and we observe a pulse broadening. This is the expected behavior since in (non-absorbing) heterogeneous media we deal with scattering attenuation. The vertical line nearby each pulse denotes the traveltime in the corresponding homogeneous (averaged squared slowness) reference medium.

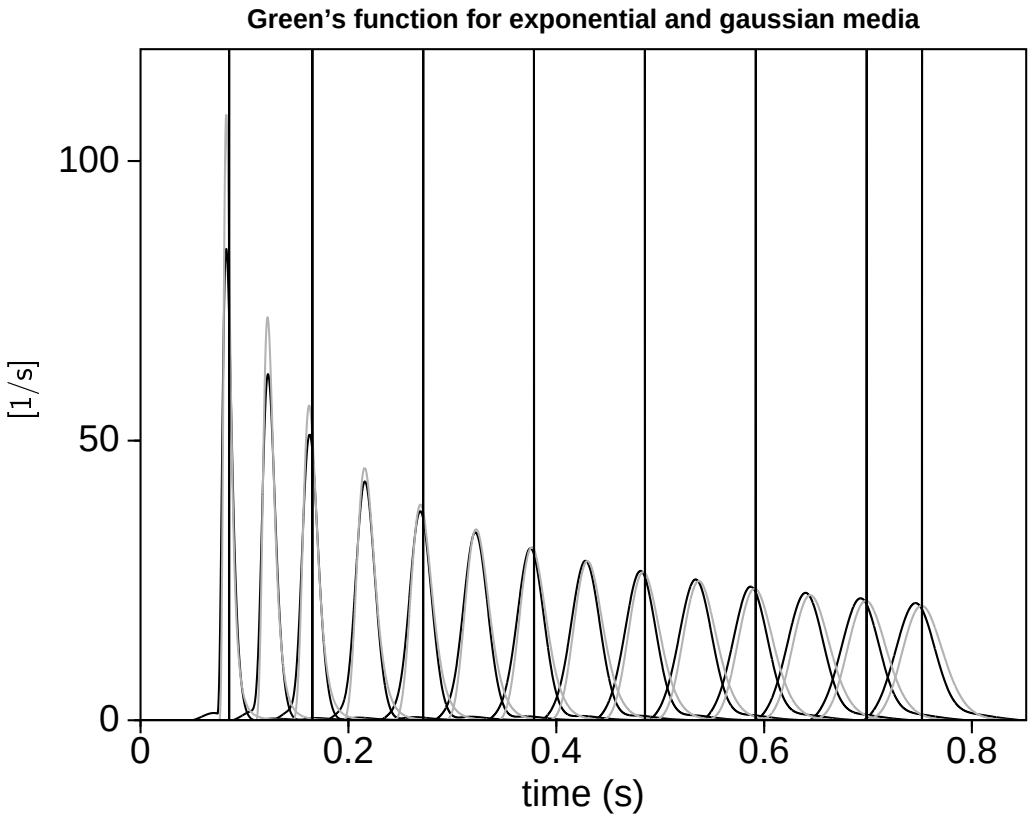

Figure 3.15: The pulses from left to right denote the Green's function for Gaussian (gray curves) and exponential (black curves) 2-D random media for travel-distances ranging from 256 to 1456m. The random medium is characterized by the standard deviation of the velocity fluctuations of 15% and a correlation length of 40m.

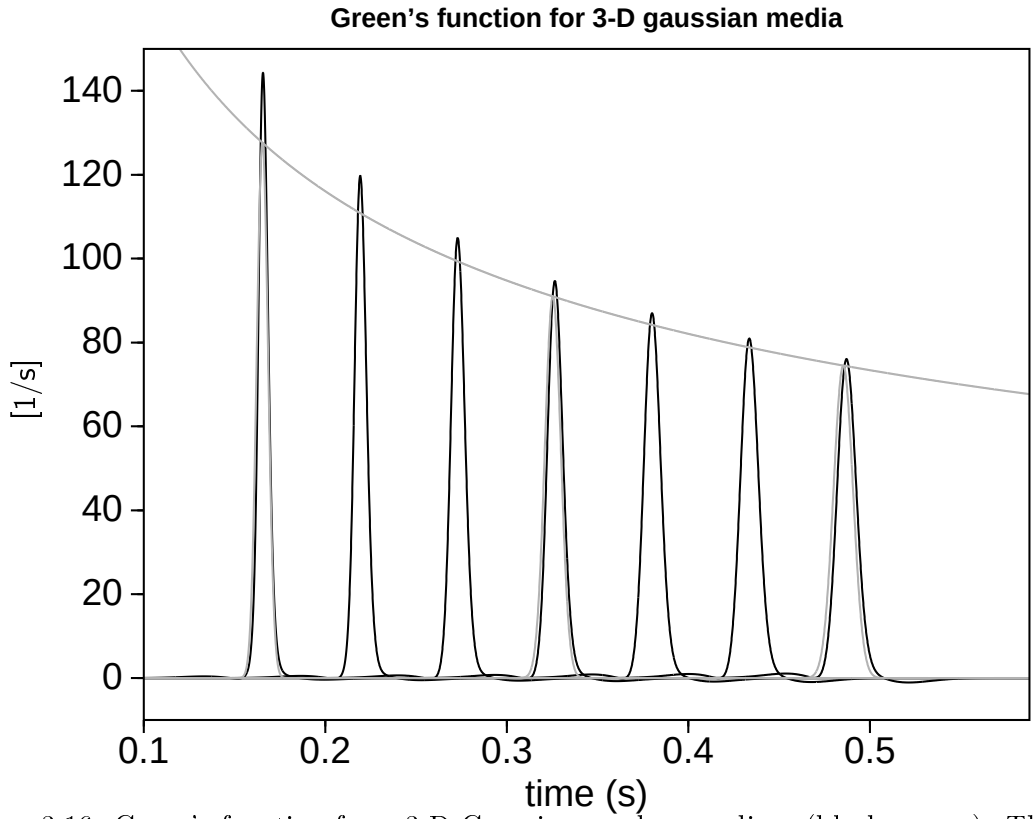

Figure 3.16: Green's function for a 3-D Gaussian random medium (black curves). The gray curves denote the Gaussian-pulse approximation (3.61) and its envelope (3.62). The travel-distances range from 496 to $1456m$, the medium is characterized by $c_0 = 3000m/s$, 5% standard deviation and by a correlation length of $40m$.

3.8 Numerical results

Now let us compare the analytical Green's function with finite-difference simulation results for wave propagation in 2-D elastic (isotropic) random media with an exponential correlation function of the velocity fluctuations (equation (2.2) approximately describes the velocity fluctuations if $|n(\mathbf{r})| << 1$). The numerical experiments and the geometry of the model have been discussed in section (2.2). The resulting synthetic seismograms are now analyzed and compared with theoretical predictions.

3.8.1 Evolution of seismic pulses and typical seismograms

The here presented theory of pulse propagation depends very much on the ratio of wavelength and correlation length λ/a. Therefore we have to consider three scenarios, namely $\lambda_0 < a$, $\lambda_0 \approx a$ and $\lambda_0 > a$, where λ_0 is the dominant wavelength of the input-wavelet. We choose in all simulation the same input-wavelet ($\lambda_0 = 40m$) and vary the correlation lengths ($a_1 = \lambda_0/4, a_2 = \lambda_0, a_3 = 4\lambda_0$) The strength of the medium fluctuations determines the spatial range of weak wave field fluctuations, where our theory is expected to work. Reported standard deviations of the velocity in reservoir geophysics and seismology are $\sigma_v = 3 - 10\%$ (Holliger & Levender, 1992, Sato & Fehler, 1998). We simulate the wave propagation in random media with 4 and 8% of standard deviation. Altogether, this results in 6 plane wave transmission experiments.

Each gray 'background' in the left-sided column of Figure (3.18) and Figure (3.19) consists of 50 traces (the z-component of the wave field) recorded on a common travel-distance gather at the corresponding depths 24, 224, 424, 624 and $824m$. The distances between geophones along the receiver line is of the order of the correlation length so that statistically (significantly) dependent measurements are avoided. From the uppermost to the lowermost seismograms in Figure (3.18) and (3.19) we clearly observe that the amplitude as well as traveltime fluctuations of traces – recorded at the same depths – increase with increasing travel-distances. This is physically reasonable since for larger travel-distances there are more interactions (scattering events) between wave field and heterogeneities resulting in a more complex wave field and consequently in more variable waveforms along the transverse distance relative to the main propagation direction. These effects are more pronounced in the more heterogeneous medium (Figure (3.19)).

There are however characteristic differences in the experiments which are worth mentioning. The complexity of the wave field around the primary arrivals and the early part of the coda (that is the time interval $t\,\epsilon\,[t_0, t_0 + 2\lambda/c_0]$, where t_0 is the first arrival time) does not only increase with travel-distance and medium's fluctuations but also with increasing correlation length (see again the left columns of Figure (3.18) and (3.19) from top to bottom). That means $u_{\mathrm{early-coda}}$ increases when $\sigma_n^2 La$ increases. In contrast to this, the later part of coda waves is larger for smaller correlation lengths, i.e., $u_{(\mathrm{later})\mathrm{coda}}$ is controlled by $\sigma_n^2 L/a$. This observation may be physically explained by the fact that forward scattering is dominant provided that $\lambda/a < 1$ and only few backscattering events delay the wave field. In a regime where $\lambda/a > 1$ forward- and backward-scattering provide a distribution of the wave field over a longer time interval. Finally, the thicker black curve denotes the result of convolving the analytically computed Green's function with the input-wavelet w(t) in the time domain $u_z(t, z) = G(t, z) * w(t)$. It seems that the theoretically predicted wave field represents the simulated wave field in a somewhat averaged form.

Our wave field description is based upon self-averaged quantities and should be able to describe the most probable ballistic wave as well as be a good approximation for the ballistic wave in typical seismograms. In order to demonstrate this, we should look for the probability densities and find those seismograms whose ballistic wave field attributes coincide with the maxima of the probability densities. Analyzing only the amplitude fluctuations, we find the probability density functions as shown in Fig. (3.17). Actually, we should take into account amplitude and phase fluctuations. Therefore, we have to compute the joint probability density function of the ballistic wave amplitudes and phases (traveltimes). Assuming statistical independence of amplitude A and traveltime t fluctuations, we can write the joint probability density p as

$$p(A,t,L) \approx p(A,L)\, p(t,L) \quad . \tag{3.64}$$

A robust estimate of $p(A,L)$ and $p(t,L)$ from the simulated data can be obtained by the maximum-likelihood method (section 2.6). The contour plots in Figures (3.20) and (3.21) display the joint probability function for the travel-distances L =24, 224, 424, 624 and 824 m. On the other hand, the diamonds in Figures (3.20) and (3.21) denote the amplitude and traveltime values as predicted by our wave field description. The filled diamonds refer to the aforesaid travel-distances. We observe that for all travel-distances these points coincide well with the maxima of the joint probability densities.

Now, the grey seismograms in right-sided columns of Figure (3.18) and (3.19) are selected in such a way that their amplitudes and traveltimes are typical ones (i.e., situated in the vicinity of the most probable amplitudes and traveltimes according to the maxima of the 2-D probability density functions in Figures (3.20) and (3.21). That is what we call typical seismograms. Of course, there are various seismograms which could be selected in this fashion. We emphasize that these typical seismograms are selected from all simulated traces without applying any averaging procedure. For the purpose of a clear illustration we show only few typical seismograms for each travel-distance (10 % of the seismograms displayed on the left side) The black curves in Figure (3.18) and (3.19) (right columns) denote the theoretically predicted ballistic wave field based on the presented Green's function. We observe a good agreement between theory and experiment for the primary arrivals. Comparing left and right plots in Figure (3.18) and (3.19) clearly demonstrates that the analytical curves give estimates of the ballistic wave fields for typical single traces.

To summarize, with help of a statistical analysis of the recorded wave fields we can verify our theoretical results. No matter if $\lambda > a$ or $\lambda < a$, the presented approach is able to predict the wave field around the primary arrivals provided that a weak scattering regime is assumed.

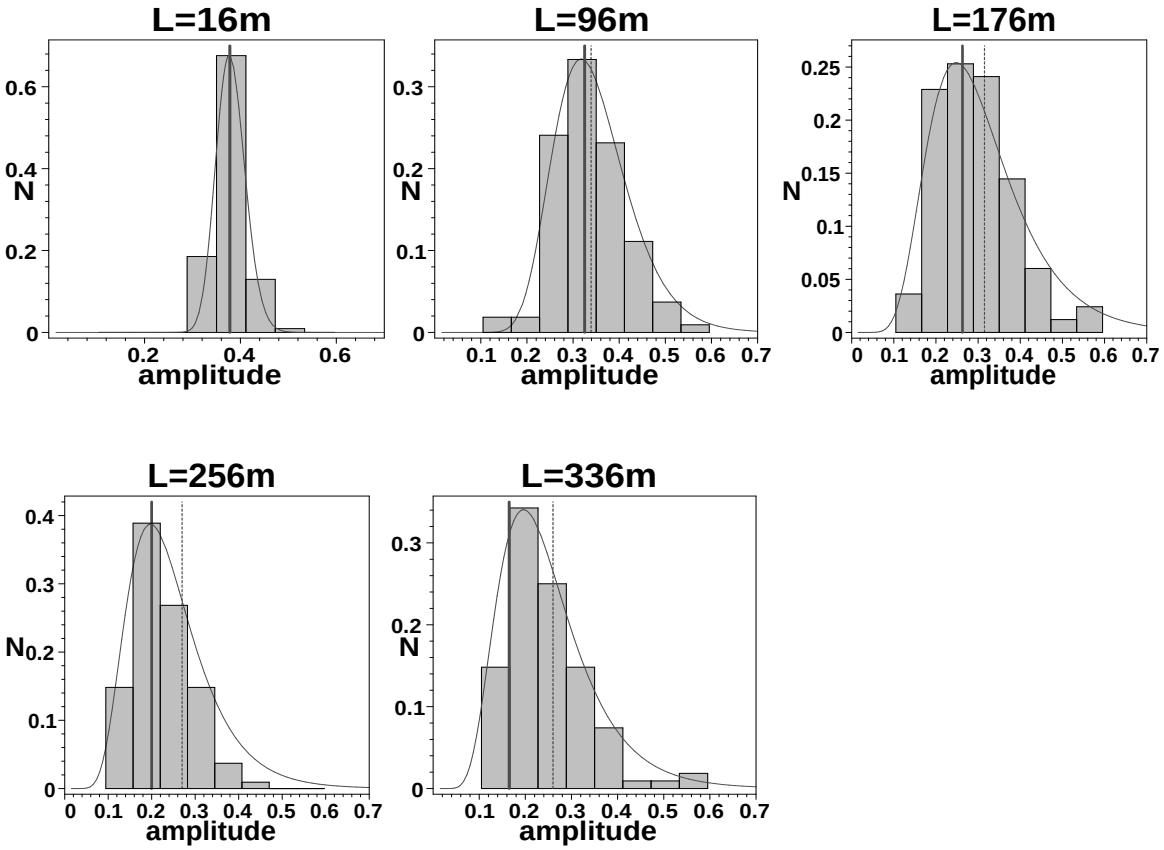

Figure 3.17: Histograms for the amplitudes of the primary wave field measured (at 108 geophones located in the transverse direction of propagation) after traveling 16, 96, 176, 256 and 336 m in the random medium characterized by $v_P = 3000m/s$, $a = 40m$, and $\sigma_n = 0.15$. The hight (occurrence) N of the grey bars denote the probability of measuring amplitudes within the interval of the bar's width. As expected, the probability density function can be approximated by the log-normal distribution (black curve). The black vertical line denotes the amplitude predicted by our theory. The latter coincides with the maximum of the probability density function (for all travel-distances); a small deviation can be seen only for $L = 336m$, where the conditions of the weak fluctuation range are not any more valid. The dashed vertical line denotes the amplitude value obtained by averaging over all measured amplitudes (this corresponds to the traveltime-corrected averaged field as discussed in section (3.8.2)).

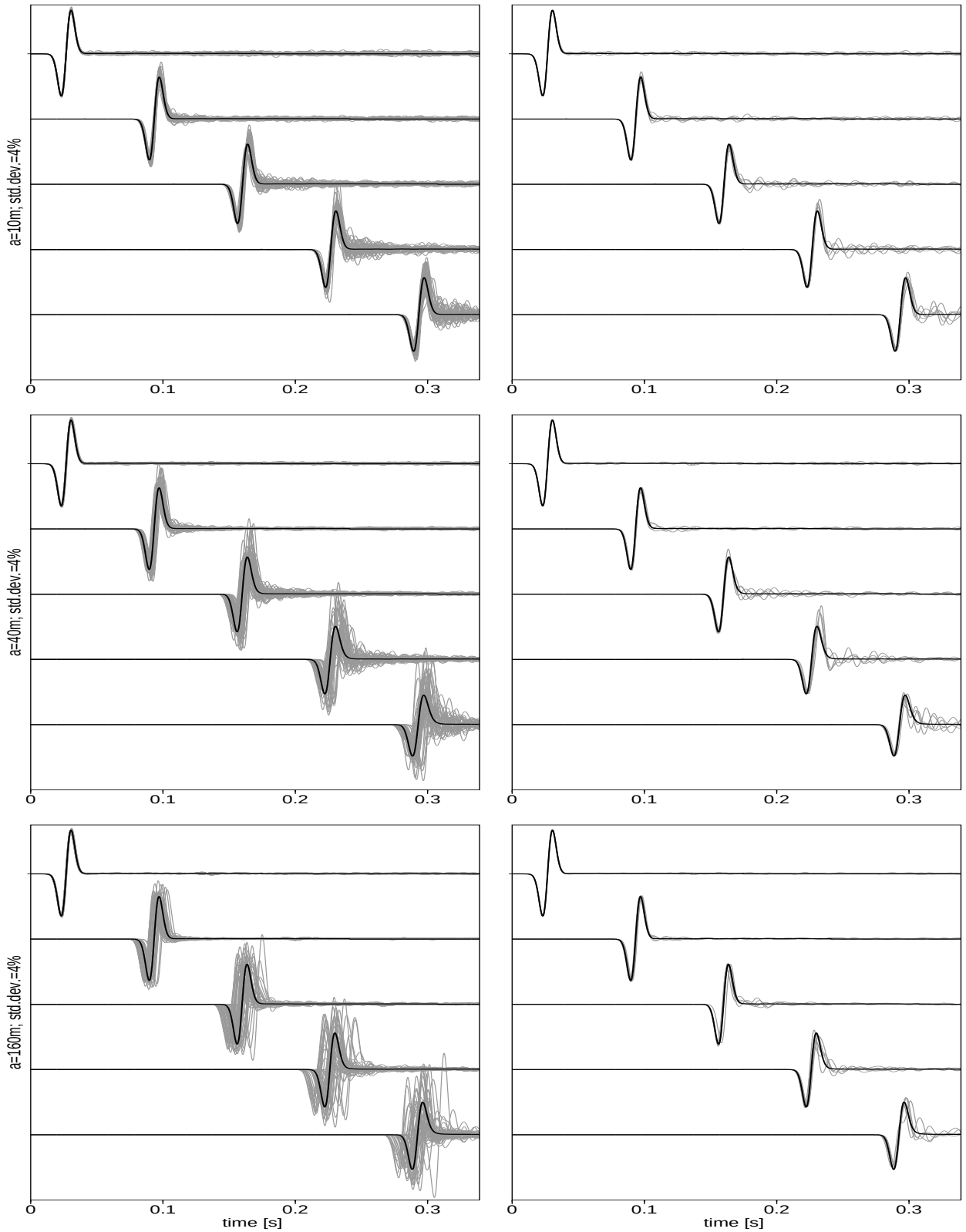

Figure 3.18: Waveforms of the numerical experiments compared with the theoretically predicted wave field for $\sigma = 4\%$ and $a = 10, 40, 160m$ (from top to bottom). The right-sided plots denote the corresponding most probable ballistic waveforms identified from the joint probability function as explained in the text.

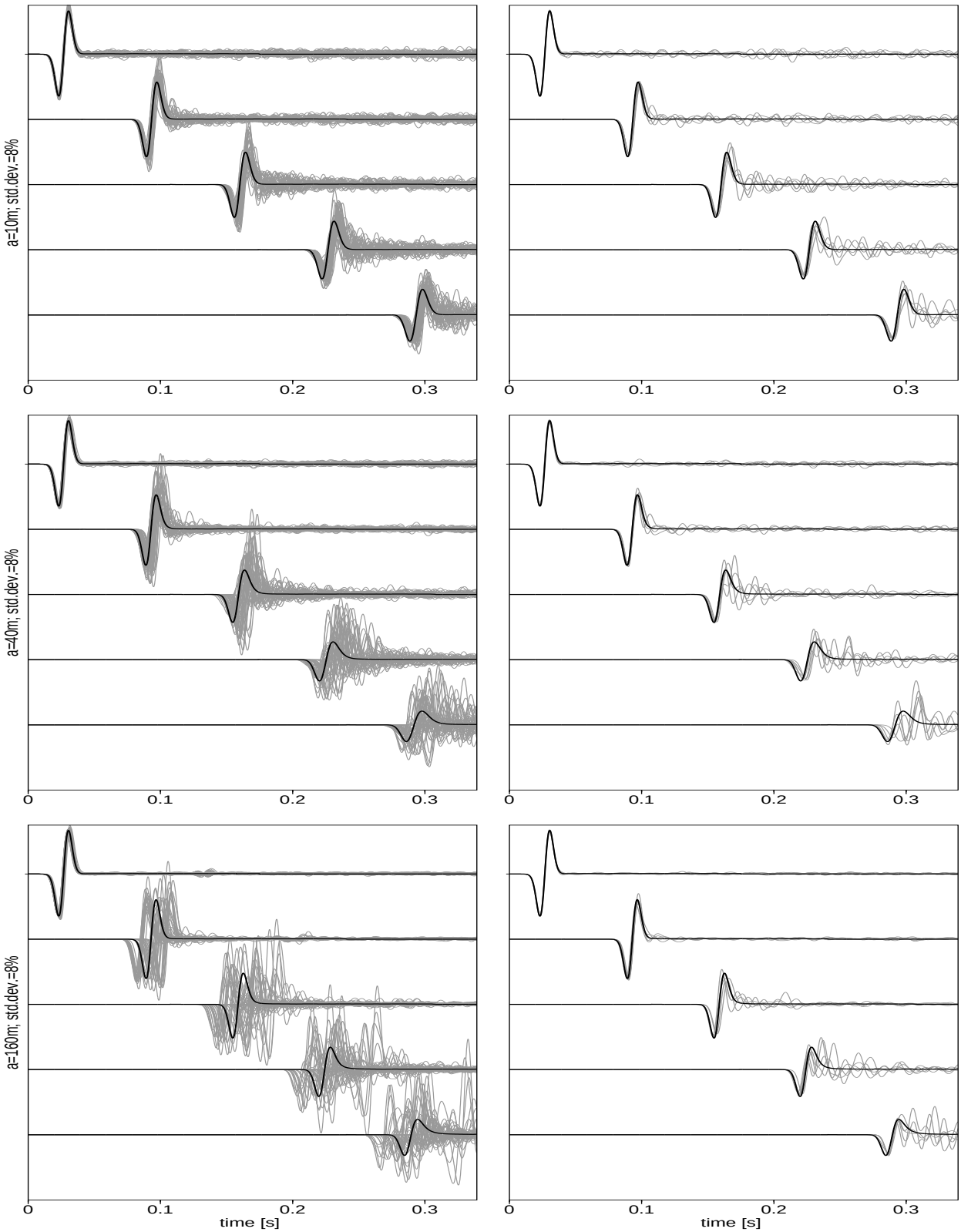

Figure 3.19: Waveforms of the numerical experiments compared with the theoretically predicted ballistic wave field for $\sigma = 8\%$ and $a = 10, 40, 160m$ (from top to bottom). The right-sided plots denote the corresponding most probable ballistic waveforms.

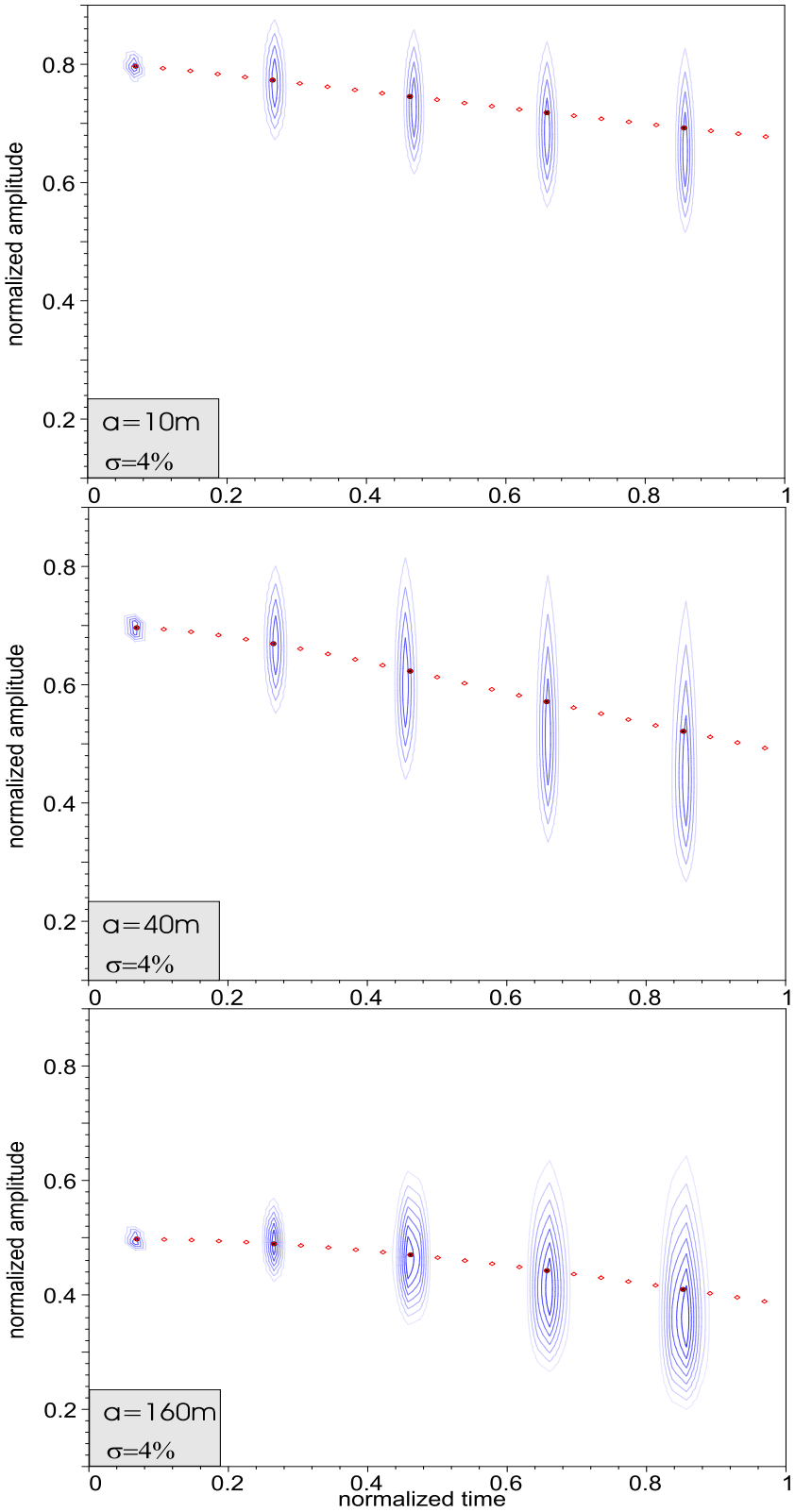

Figure 3.20: The contour plots show the reconstructed amplitude/phase joint probability densities for the travel-distances $L = 24, 224, 424, 624, 824m$ corresponding to the displayed seismograms in Figure (3.18). The filled diamonds represent the theoretically predicted amplitude and traveltime of the ballistic wave and correspond to the black curves in Figure (3.18). In all cases these filled diamonds are located in the center (or at least in the vicinity) of the innermost contour denoting the maximum of the joint probability density function.

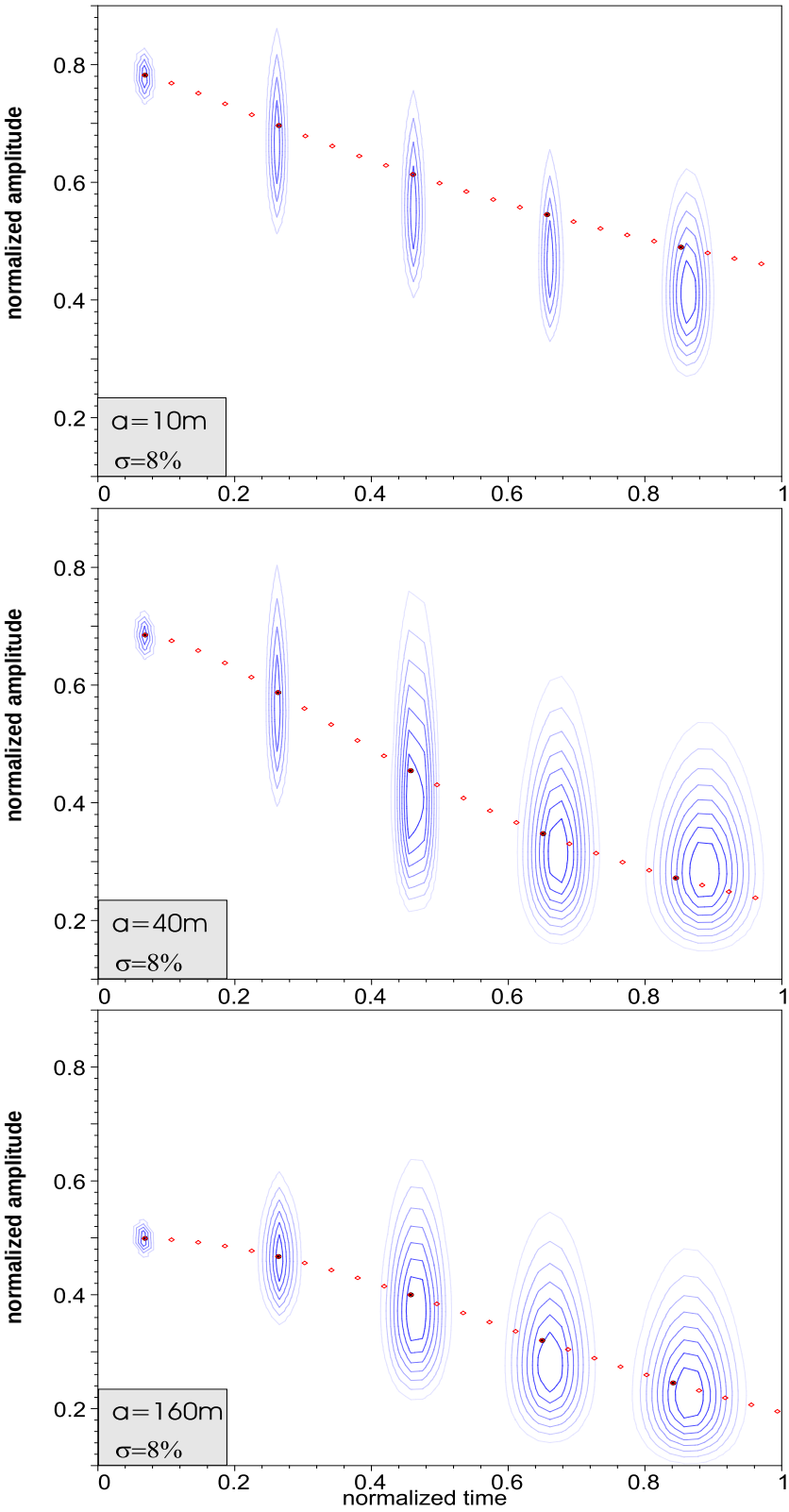

Figure 3.21: The contour plots show the reconstructed amplitude/phase joint probability densities for the travel-distances $L = 24, 224, 424, 624, 824m$ corresponding to the displayed seismograms in Figure (3.19). The filled diamonds represent the theoretically predicted amplitude and traveltime of the ballistic wave and correspond to the black curves in Figure (3.19). In all cases these filled diamonds are located in the center (or at least in the vicinity) of the innermost contour denoting the maximum of the joint probability density function.

3.8.2 Relation to the averaged traveltime-corrected field

Further, we investigate the relationship between the ODA formalism and usual averaging formalisms. When studying exclusively scattering attenuation, there are recipes that improve the averaging by corrections of the traveltime fluctuations. Sato and Fehler (1998) describe a method that takes into account the traveltime shift due to long-wavelength components of the velocity fluctuations. A decomposition of the fluctuations into long- and short-wavelength components and then the application of the Born approximation lead to the so-called 'traveltime-corrected Born approximation' which is expected to describe the frequency dependence of measured quality factors from various data sets (see their Figure 5.11).

In Figure (3.22) we calculate the mean field (dashed curve) by simply stacking all traces without any corrections. Except for very small travel-distances ($L < a$), we observe a big difference between the mean field waveform and our wave field approximation (black solid curve). The strong mean field attenuation is a statistical effect, since the averaging is performed over all traces of a given seismogram regardless of the traveltime fluctuations. Wu (1982) found that the mean field attenuation is not necessarily related to the scattering attenuation of seismic waves in a real heterogeneous medium. For travel-distances smaller than the characteristic size of heterogeneity, both wave field descriptions coincide (uppermost seismogram in Figure (3.22)) since in this range almost no wave field energy is transferred into the incoherent wave field. We conclude that our approach goes beyond the ordinary mean field description, where all incoherent parts of the wave field are removed.

In the same Figure, the gray curves denote the traveltime-corrected sections obtained by stacking after the traces are shifted towards a mean traveltime (see illustration (5.6) of Sato and Fehler, 1998). As picking criterion we used the first zero-crossing after the first waveform extremum. We observe a rather good agreement of our results with the traveltime-corrected section for small travel-distances. For larger travel-distances, the traveltime-corrected averaged field predicts larger amplitudes than the generalized O'Doherty-Anstey formalism. This is not surprising since our wave field description is based on the mean of log-amplitude and phase fluctuations. More precisely, using the averaged phase $\langle\phi\rangle$ implies the traveltime correction in a natural way. Moreover, the averaged traveltime-corrected wave field can be written

$$\begin{aligned} u_{ttc} &= \langle |u| e^{i\langle\phi\rangle} \rangle && (3.65)\\ &= \langle |u| \rangle e^{i\langle\phi\rangle} && (3.66)\\ &= e^{\ln\langle |u| \rangle + i\langle\phi\rangle} \quad . && (3.67) \end{aligned}$$

Using the Rytov approximation, Shapiro and Kneib (1993) obtained:

$$\ln\langle |u| \rangle = -\frac{1}{2}\sigma_{\chi\chi}^2 \quad . \tag{3.68}$$

Thus, equation (3.68) defines the scattering attenuation coefficient of the traveltime-corrected wave field formulated in the Rytov approximation . Comparing this result with equation (3.29), it is obvious that the attenuation given by the generalized O'Doherty-Anstey formalism is approximately twice the attenuation corresponding to the traveltime-corrected and averaged section (at least for the frequency range $ka > 1$). This explains the different amplitudes in Figure (3.22). In contrast to χ, $|u|$ is not a self-averaged quantity and therefore does not correspond to the most probable seismogram. This is also indicated in Figure (3.17) by

the dashed vertical lines denoting amplitudes of the traveltime-corrected averaged field. The latter move away from the maxima of the histograms for increasing travel-distances.

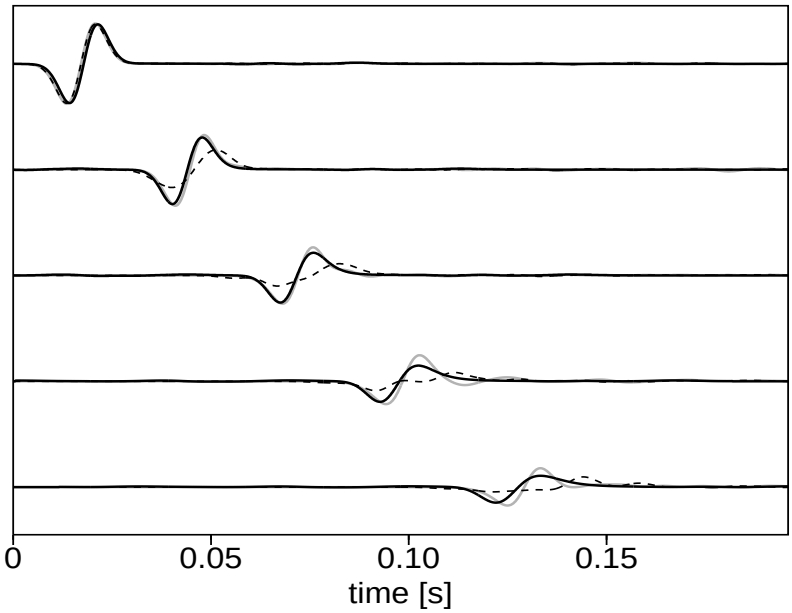

Figure 3.22: For the same FD-experiment we computed the mean field (dashed curve), the traveltime-corrected section (gray curve) and the generalized ODA wave field description (solid black curve). The traces are shown for the wave field traveled 16, 96, 176, 256 and 336m. The parameters of the medium are given in the description of Figure (3.1).

Another dynamic-equivalent medium approach was proposed by Fang and Müller (1996). They derived minimum-phase attenuation operators based on the Kramers-Kronig relationship between attenuation and dispersion of transients and describe the traveltime-corrected sections for the same kind of transmission experiments very well. However, their calculation of attenuation implicitly requires an assumption for the scattering angle, which in turn can be only determined by numerical tests. This scattering angle is travel-distance dependent as shown by equation (3.56). It can fluctuate in different realizations of random media (it depends on the statistical properties and probability distribution) and therefore it is a realization dependent wave field description. Moreover, their scattering attenuation operator is based on a single scattering approximation which is inferior compared with multiple scattering approximations used in order to derive equations (3.29) and (3.30). Thus, all these shortcomings can be avoided when using self-averaged wave field attributes as it is done for the here proposed Green's function (3.57).

3.8.3 Estimates of scattering attenuation

In order to obtain scattering attenuation estimates we apply the so-called spectral decay method using the seismograms of 3-D finite-difference simulations in elastic random media. The random medium realization in this experiment is characterized by an exponential correlation function with $a = 45m$ and $\sigma_v = 5\%$ superimposed on the P-wave velocity $v_P = 3000m/s$. The S-wave velocity and density model are derived from the P-wave velocity model using empirical relations for reservoir sandstones ($v_S = 0.61v_P - 314$ and $\rho = 0.22v_P + 1498$, see also Bohlen and Milkereit, 2001). The dominant frequency of the input-wavelet is $f = 70Hz$.

More specifically, we consider the decay of the logarithm of amplitude spectrum with travel-distance. The slope of the regression line is then directly linked with a global scattering Q estimate by $Q^{-1} = \frac{2\alpha}{k}$ where $\alpha = -\frac{\ln(A(\omega))}{L}$ with the amplitude spectrum $A(\omega)$ of the wave field. However, care should be taken how the analysis is done. Shapiro and Kneib (1993) investigated the influence of the different processing steps. Stacking all seismograms of the common-travel-distance gather in the time domain and analyzing the logarithm of the amplitude spectra vs. L, yields the the mean field attenuation. Averaging the amplitude spectra and then analyzing its logarithm vs. L corresponds to the traveltime-corrected attenuation estimate ${}^{ttc}Q^{-1} = -\frac{2}{k}\frac{\ln(\langle A(\omega)\rangle)}{L}$, where the angular brackets denote the averaging operator. Changing the order of operations, we obtain the scattering attenuation estimate corresponding to the mean of the log-amplitude spectra $Q^{-1} = -\frac{2}{k}\frac{\langle\ln(A(\omega))\rangle}{L}$. Note that strictly speaking it is not correct to apply a linear regression to obtain Q^{-1} and interpreting the result with equation (3.39) because of its travel-distance dependency. However, restricting the analysis to an intermediate depth range (i.e. respecting the validity range of eq. (3.39)), where the wave field fluctuations are not at all saturated, we obtain reliable estimates.

Moreover, the determination of Q^{-1} values from the first arrivals in seismograms is very sensitive to the applied window length around the primary arrivals (see e.g. Frenje and Juhlin, 2000). We applied a window length being equal to the dominant source wavelength for $L = 0$ and that increases linearly with L to account for the broadening and the traveltime fluctuations of the primary wave field. According to the Gaussian pulse approximation in section (3.7.2), the window length should increase with $\sqrt{L}$ (in this numerical analysis a linear increase with travel-distance is used, which provided practically the same estimates as the $\sqrt{L}$-increase).

The resulting Q^{-1} estimates are shown in Figure (3.23) as a function of frequency. Increasing the window length produces lower Q^{-1} since parts of the coda are included in the analysis. We note that within the investigated frequency range $5 \leq ka \leq 10$, the trend of increasing ${}^{ttc}Q^{-1}$ with increasing ka remains unaffected by the window length. In that frequency range the traveltime-corrected scattering attenuation estimate (3.68) and that of the scattering attenuation model (3.39) differ only by a factor 2. However, the above described procedure to numerically determine Q^{-1} gives more stable results for the traveltime-corrected scattering attenuation estimate. This can be seen in Figure (3.23), where the traveltime-corrected scattering attenuation estimate closely mimics the theoretical curve (blue curve), whereas the agreement between experiment and theory for Q^{-1} from the mean of log-amplitude spectra is poor (green curve, crosses).

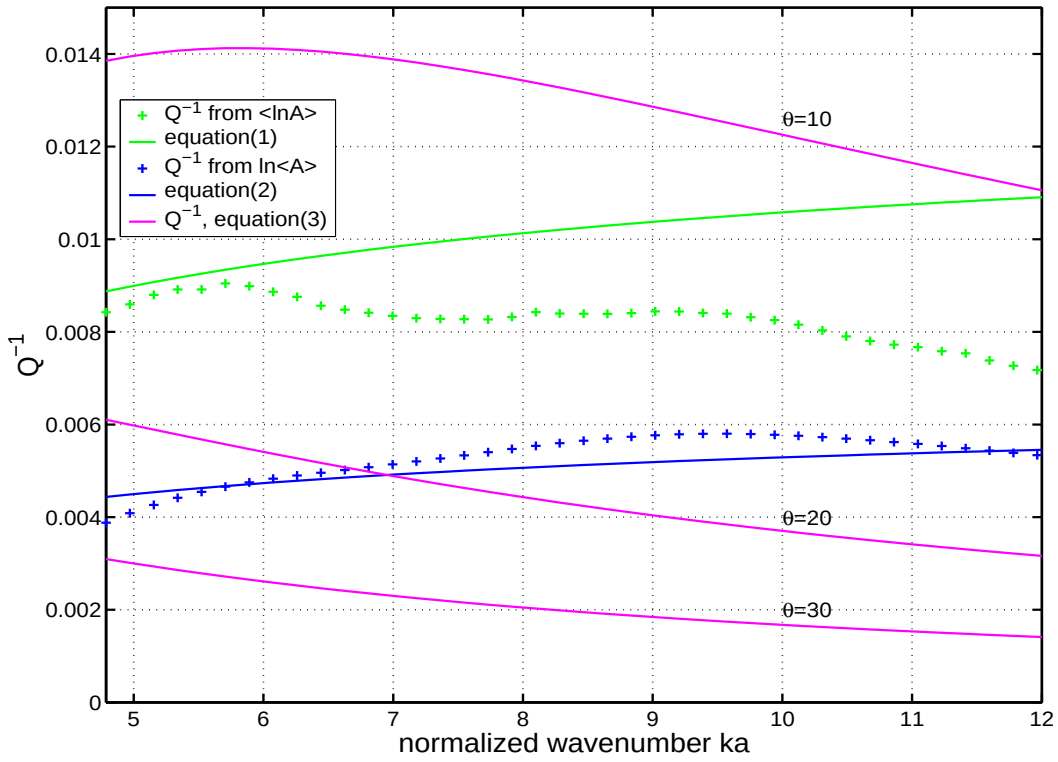

Figure 3.23: Estimated Q^{-1} values as a function of ka from synthetic data versus theoretical predictions. The green and blue curves correspond to equations (3.39) and (3.68), respectively. Scattering attenuation estimates using equation (3.54) are plotted for the scattering angles $\vartheta = 10, 20, 30^o$ (red curves). The best agreement between theory and experiment concerning magnitude and frequency dependence of Q^{-1} is obtained for the traveltime-corrected theory based on the Rytov approximation.

According to equation (3.56) this implies a scattering angle of 20^o when using equation (3.55), i.e., the traveltime-corrected scattering attenuation estimate in the formulation of Sato (see also the red curves in Figure (3.23)). The red curves suggest scattering angles $\leq 20^o$. This result is in full agreement with that of Frenje and Juhlin (2000), who also obtained scattering attenuation estimates from finite-difference simulations in 3-D acoustic random media and could explain them with scattering angles $\leq 20^o$. Note that the frequency dependence suggested by the traveltime-corrected model of Sato is opposite to the theoretical prediction.